University of Alberta

Characterization of Stable Delamination Growth in Fiber-reinforced Polymers using Analytical and Numerical approaches

by

Tsegay Belay

A thesis submitted to the Faculty of Graduate Studies and Research in partial fulfillment of the requirements for the degree of

Master of Science

Department of Mechanical Engineering

Spring 2013
Edmonton, Alberta

Abstract

This thesis discusses methodologies for the prediction of stable delamination development in fiber-reinforced composites in pure fracture modes using analytical and numerical methods.

A new test method, named internal-notched-flexure (INF) test, has recently been proposed to quantify mode II interlaminar fracture toughness of fibre composites. Previous investigation has shown that unlike any of the existing test methods, the INF test generates unconditionally stable delamination growth. This thesis discusses a follow-up study that revises the analytical expressions for compliance (C) of INF specimen and its energy release rate for delamination (G). The main improvement in the current approach is to take into account load in the overhanging section of the specimen; while in the previous approach, the overhanging section was assumed to be load-free. Validation of the revised expressions is through comparison of the initial specimen stiffness with that from a finite element (FE) model of the INF specimen. The virtual INF specimen has cohesive elements in the interlaminar region to simulate the delamination growth, from which extent of damage in front of the crack tip can be quantified. Results from FE model suggest that an extensive damage exists at the crack tip before delamination growth commences. Therefore, the use of a physical crack length in the analytical expression for G may severely overestimate the interlaminar fracture toughness. Instead, an effective crack length should be used. Expression for G based on the effective crack length yields a value that is very close to the input critical energy release rate (G_c) for the cohesive elements. The study concludes that load in the overhanging section should be considered for deriving the analytical expressions for C and G of the INF specimen, and

an effective crack length should be used to calculate the G_c value from the analytical expression.

In addition to the above work, the study also touches on a finite element approach based on continuum solid elements with an elastic-plastic damage material property. The approach was proposed to simulate crack growth in the interlamianr region of FRP, but should also be applicable to other crack growth phenomena. In this approach, solid elements are used to simulate crack growth, based on criteria that are a combination of all stresses, in order to take into account the effect of in-plane normal stress on the damage initiation. The criterion for delamination propagation is defined based on critical strain energy. The approach was implemented in a finite element code and was applied to pre-cracked composites to illustrate its feasibility to simulate the crack development.

Acknowledgements

I am very grateful to my supervisor, Dr. Jar and co-supervisor Dr. Cheng, for their guidance throughout the course of my MSc study. Without their unreserved support, continued advice and valuable suggestions on critical problems, it would have been difficult to complete my study. I also would like to extend my sincere thanks to my friends Souvenir Mohammed, Scott McKinney, Zahou Yang and Feng Yu for their encouragement and help. Finally, I express my heartfelt gratitude to my family for their unreserved love and constant encouragement during my whole life.

Table of Content

List of Figures

List of Tables

List of Symbols

a_1	crack length, measured from loading pin to furthest crack tip position
a_2	crack length, measured from loading pin to nearest crack tip position
a_e	effective crack length
C	compliance
c	half ligament length in DENT test
d	damage parameter
E	Young' modulus of elasticity
E_{11}	Young' modulus of in local 1-direction
E_{ijkl}	component of the elasticity tensor
F_{1B}^c, F_{2B}^c	concentrated shear forces at the crack tip point B on top and bottom halves of a beam respectively
F_{1D}^c, F_{2D}^c	concentrated shear force at the crack tip point D on top and bottom halves of a beam respectively
F_{1KA}, F_{2KA}	interlaminar shear force in the overhanging sections *KA* on top and bottom halves of a beam respectively
F_{1DE}, F_{2DE}	interlaminar shear force in the overhanging sections *DE* on top bottom halves of a beam respectively
G	energy release rate
G_{a1}	energy release rate, associated with crack growth in $a1$ direction
G_{a2}	energy release rate, associated with crack growth in $a2$ direction
G_C	critical energy release rate
G_{IC}, G_{IIC}	mode I or II critical energy release rate
h	beam thickness
k	Shear force deformation correction factor in beams
L	half span length of INF test
l	length of INF specimen
$N(x)$	axial force
P	concentrated force

Q	shear force
S	shear strength
Y	tensile strength
T_0	original thickness of cohesive zone
U	strain energy
U_0	Strain energy at damage initiation point
U_C	Critical strain energy
U_d	Dissipated energy during damage process
$\mathbf{u}$	displacement vector
u, v, w	displacement in the x-, y- or z-direction
u_1, u_2, u_3	displacement in the 1-, 2- or 3-direction
u_0	displacement on the neutral axis in the x-direction
w	width of a beam
w_0	displacement on the neutral axis in the z-direction
α	coefficient parameter in damage intitiation criteria
$\gamma,\ \gamma_{xy}$	shear strain
δ_i	associated displacements with top and bottom halves of a beam
κ	curvature
μ	shear modulus
ν	Poisson's ratio
$\psi(x)$	beam rotation angle
ε_{ij}, ε	strain components and strain tensor
ε_{11}, ε_{22}, ε_{33}	normal strains in x-, y- and z-direction
ε_y	yielding strain
σ_{ij}, $\boldsymbol{\sigma}$	Cauchy stress components and stress tensor
σ_{11}, σ_{22}, σ_{33}	normal stresses in x-, y- and z-direction
σ_y	yielding stress
τ	shear stress
ν_{11}, ν_{23}, ν_{13}	Poison's ratio in orthotropic elastic materials

Chapter 1 Introduction

1.1 Background

Composite materials consist of two or more different constituents which are combined together to create a superior and distinct material. These constituents are divided into matrix and reinforcement. The reinforcements which are usually small in size provide strength and rigidity to the new material. The matrix is a lightweight, lower-strength material which serves as a support to hold the reinforcement together and protect them from scratches that might generate to damage at a low stress level. It also acts as a media to transfer load among individual reinforcement. For example, the combination of fiber glass with polymer creates a unique material called fiber-reinforced polymer (FRP) and has properties unachievable by each component.

Advanced FRPs have been widely used in aerospace, automotive, construction and other industries because of their superior mechanical properties such as light weight, high specific stiffness and strength. However, unexpected excessive loading, manufacturing defects, shocks and low velocity impact can cause crack initiation and growth between layers, commonly known as in the interlaminar region. Damage or separation in the interlaminar region is called delamination which is one of the major failure modes in FRP to degradation of stiffness, which can lead to loss of effective

service lifetime or catastrophic failure of structures [1]. As a result, much of research has been done in the last two decades, in order to develop accurate analytical and numerical models that are able to predict delamination development in FRP.

The delamination process commonly involves two stages: initiation and growth. Delamination initiation is related to the interfacial strength of the material and in many applications stress-based criteria are used to predict its occurrence [2]. Delamination growth has been widely investigated based on fracture mechanics. Both analytical and numerical methods are used to calculate fracture-related parameters such as energy release rate (G), stress intensity factor (K) or J-integral (J) that serves as a driving force for the crack growth. Methods such as compliance derivative technique (CDT) [3-4], virtual crack closure technique (VCCT) [5] or J-integral [6-7] can be used to calculate the energy release rate (G), and to predict delamination growth by comparing G values to the critical value (G_C) for fracture. However, all of these techniques cannot be directly applied to prediction of delamination without an initial crack.

Further complication of the finite element implementation arises when progressive delamination is involved. An alternative solution to avoid the above difficulties is to use cohesive elements [8-9]. A cohesive damage zone is developed near the crack front and the crack growth is described by adopting a softening relationship between traction and relative displacement, with the area under the curve being the critical fracture energy. Computational issue of cohesive crack model has been extensively investigated by Alfano et al. [10].

1.2 Purpose and scope of research

Purpose of this research is to study stable delamination growth in fiber composites using analytical and numerical approaches. The analytical approach will be used to characterize detailed delamination growth in FRP under pure fracture mode II. This approach will provide essential information on parameters that govern the delamination growth, such as the extent of damage in front of the crack tip, and the influence of physical and effective crack lengths in calculating energy release rate, and the speed and extent of delamination growth. The information, is of great interest to structural engineers, and can facilitate design of reliable and safe fiber composite structures.

Another essential property of delamination is the fracture toughness which can be characterized by partitioning the fracture process into three modes: mode I (opening), mode II (shear) , and mode III (tear). The critical energy release rates under those modes of fractures can be measured experimentally through appropriate testing methods. In this study, a critical energy release rate (G_{IIC}) obtained from a previous experimental investigation on internal-notched flexure (INF) test, is used in the finite-element (FE) based prediction of delamination onset and growth. It should be noted that the FEM work described in this study is based on continuum solid element with physically meaningful criteria for delamination simulation. The use of solid elements will enable us to take into account all stress components in determining the initiation of delamination.

1.3 Structure of thesis

The thesis is divided in two main parts. The first part concentrates on the analytical approach to predict stable delamination growth in pure mode II fracture, Chapter 2. The development of an accurate analytical model is a vital tool for predicting delamination growth in FRP. The analytical expressions for compliance (C) of the INF specimen and its energy release rate for delamination (G) are derived. The second part is concerned about finite element simulation of delamination, chapter 3. This chapter provides a basis for understanding various methods that are conventionally used to simulate delamination in FRP. Discussion also includes some details of the new proposed damage material model for delamination simulation.

The last chapter gives a summary of the whole work and identifies problems that can be considered for the future work.

Chapter 2 Analytical Prediction of Stable Delamination Growth in Internal-Notched Flexure (INF) Test

2.1 Introduction

The delamination process in fiber composites can be characterized by partitioning the fracture process into three pure modes: the opening (mode I), the in-plane shear (mode II) and the out-of-plane shear (mode III). The interfacial fracture toughness (G_C) of composites in each mode is different due to the difference in fracture mechanisms and extensive efforts have been made to devise methods for measuring the critical energy release rate under mode I and mode II loading with very carefully designed experiments. This is because firstly G_{IC} and G_{IIC} are the most important parameters to evaluate the performance of fiber composites' resistance to fracture and secondly they are essential input quantities for simulating delamination growth using FEM. The study on delamination in mode III, on the other hand, has received little attention. Delamination growth is assumed to take place when the energy release rate reaches a critical value. Since the change of energy release rate with crack growth can also be used to determine whether the delamination growth is stable analytical expression for the energy release rate is very important in the study of delamination propagation.

While the development of mode I delamination test is successful and standardized [11] using the double cantilever beam (DCB) test, as shown in Figure 2.1(a), there is a long and winding road to standardize mode II delamination [12]. The four most commonly

used test methods to characterize mode II delamination fracture toughness are: end-loaded split (ELS), end-notch flexure (ENF), including the stabilized version, and four-point bend ENF (4ENF) tests, as shown in Figures 2.1(b) to 2.1(d). At the time when this thesis is prepared, none of the above methods has been accepted as the standard due to uncertainty of crack growth stability during the test. In addition significant data scatter and sometimes complicated test set-up are also drawbacks for some of those tests. Note that all of those tests adopt beam-shaped specimen geometries with a pre-crack, of which a brief history is summarized in ref. [13].

(a)

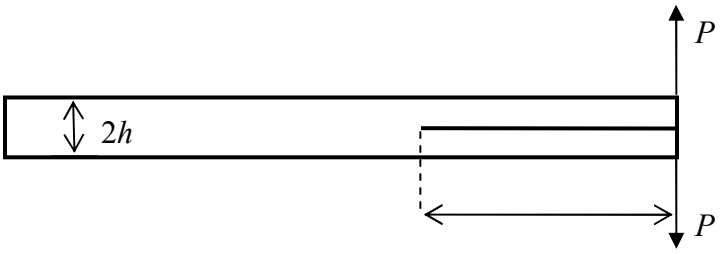

(b)

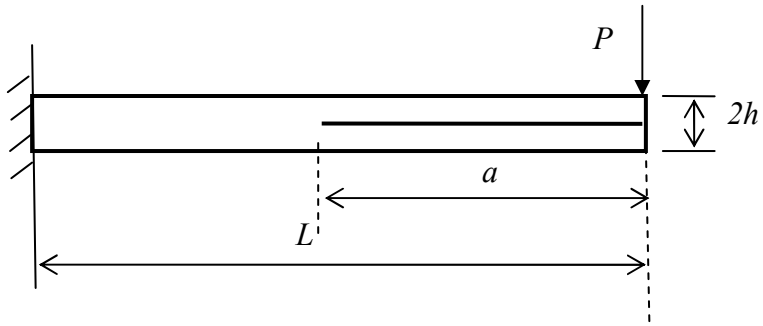

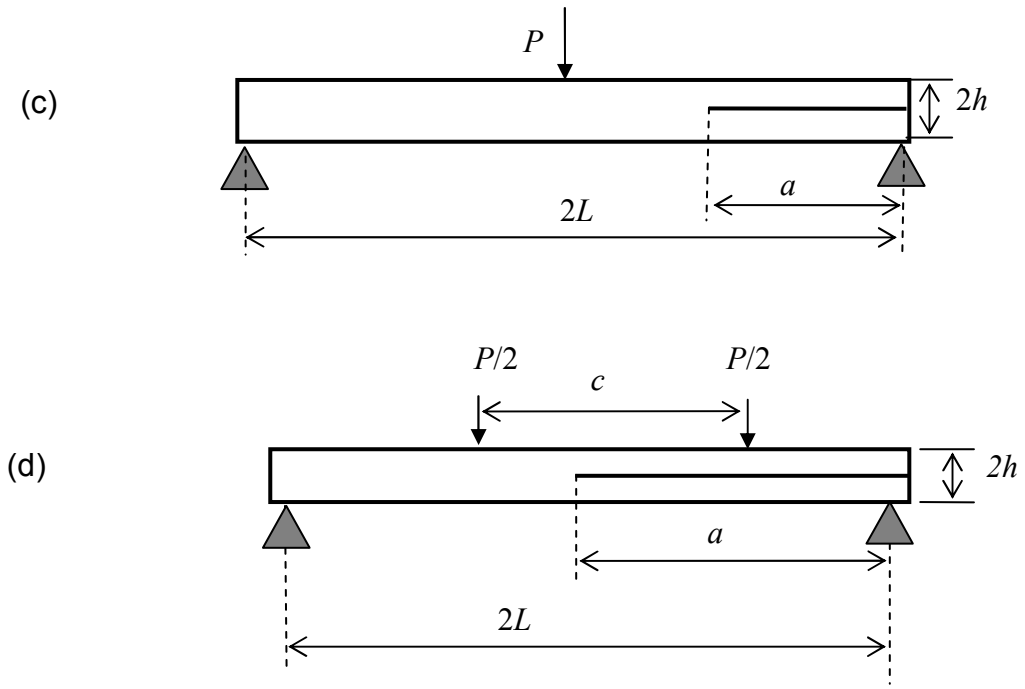

Figure 2.1. Schematic diagram of (a) DCB, (b) ELS, (c) ENF, and (d) 4EN

A new test method, named internal-notched-flexure (INF) test, has been reported in a previous paper [14] to quantify delamination resistance of fibre-reinforced polymers (FRP) when subjected to transverse loading. Figure 2.2(a) shows the INF test setup that applies three-point bending to a specimen that contains an embedded insert film at mid-thickness. Although INF test is very similar to central-notched-flexure (CNF) test [15] as shown in Figure. 2.2(b), in both specimen design and loading mode, the INF test has the transverse load applied un-symmetrically with respect to the insert film; while the CNF test has the transverse load applied symmetrically with respect to the insert film. In addition, the CNF test requires the insert film to be placed within the two supports; while the INF test requires one end of the insert film (i.e. point D in Figure. 2.2(a)) to be outside the span, and the other end (i.e. point B in Figure 2.2(a)) very close to the central

transverse load. The previous work [14] shows that with a proper choice of a_2 value, delamination growth starts from point D without any crack development from point B.

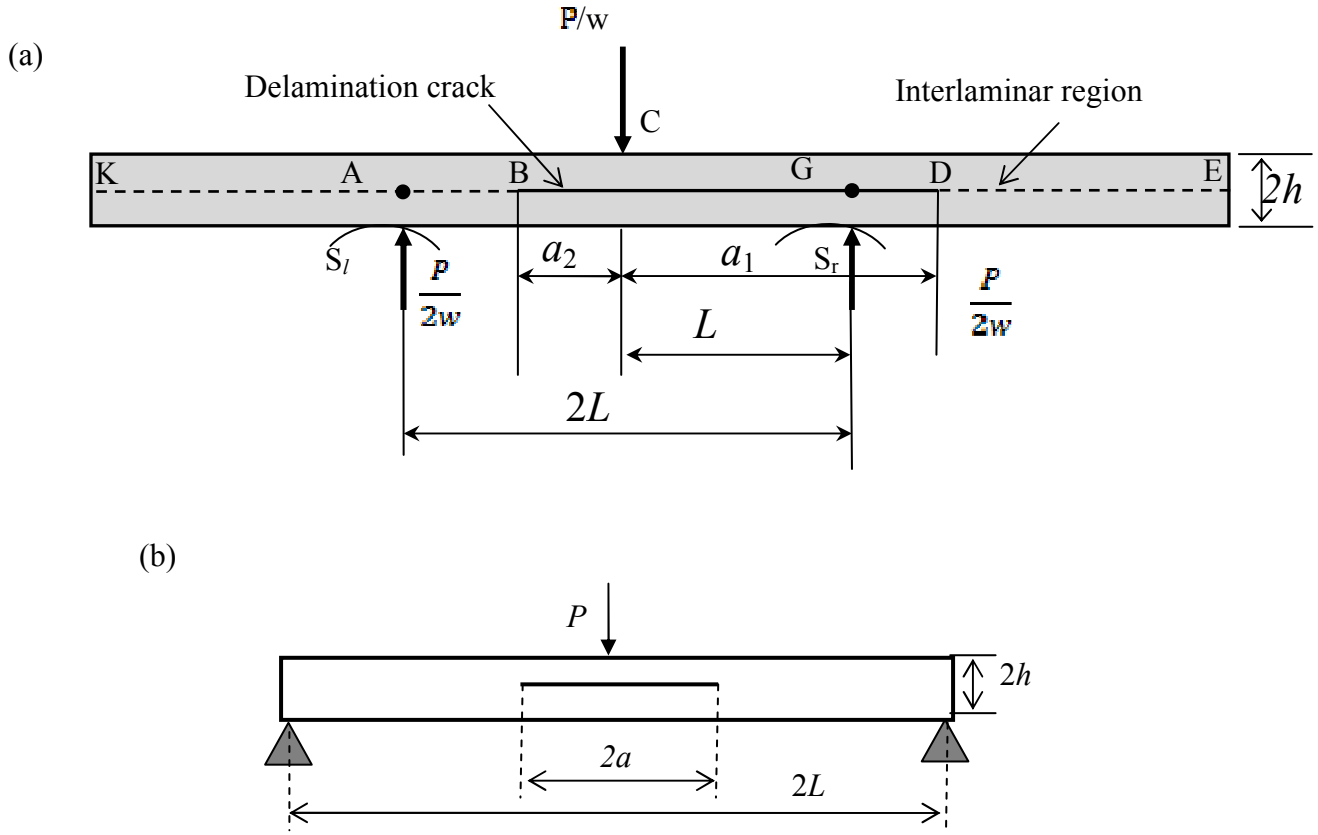

Figure 2.2 Schematic diagram of (a) INF test methods under three point bending, and (b) CNF test.

Major advantage of INF test over the other tests is its unconditionally stable delamination growth. This is due to the continuous force increase during the test, even after delamination growth has started, as depicted in Figure 2.3. For the other tests, the load either decreases, such as in end-notched-flexure (ENF) and end-loaded-split (ELS) tests, or at best, maintains at the same level, such as in (4ENF) test [13]. Figure 2.3 presents a comparison among those test results, which suggests that stability in delamination growth is in the order of INF > 4ENF > ELS > ENF.

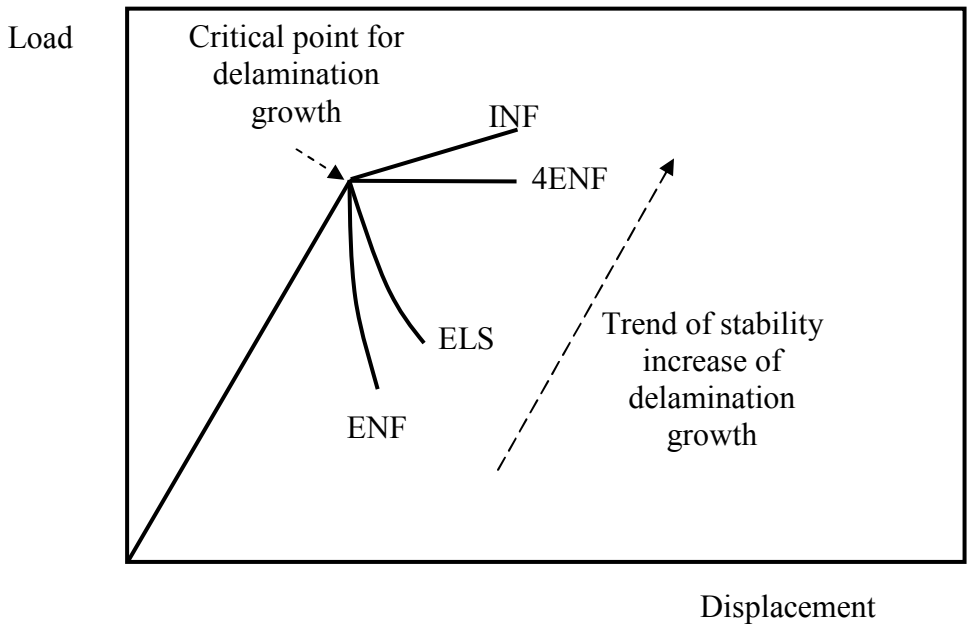

Figure. 2.3. Schematic diagram of load-displacement plots from five mode II delamination tests [14]

Previous approach [16] to derive the analytical expressions for compliance and energy release rate of the INF test, as given by Eqns. (2.1-2.3) below, is based on the approach proposed by Maikuma et al. [15].

$$C_{ref.[16]} = \frac{\delta}{P} = \frac{L^3}{4Eh^3w} + \frac{L}{4\kappa\mu hw} + \frac{3\left(-3L^4-8a_2L^3+4a_1L^3+6a_2^2L^2+12a_1a_2L^2-12a_1a_2^2L+4a_1a_2^3+a_2^4\right)}{32Eh^3w(a_1+a_2)} \tag{2.1}$$

$$G_{a_1,ref.[16]} = \frac{9P^2}{64Ew^2h^3(a_1+a_2)^2}[a_2^2 - 2a_2L - L^2]^2 \tag{2.2}$$

$$G_{a_2,ref.[16]} = \frac{9P^2}{64Ew^2h^3(a_1+a_2)^2}[a_2^2 + L^2 - 2a_1L + 2a_1a_2]^2 \tag{2.3}$$

where C is the compliance, δ displacement at the central point at which transverse load P is applied, G_{a_1} and G_{a_2} the energy release rate for delamination growth from right and left crack tips, i.e. points D and B in Figure 2.2, respectively, E flexural modulus of the

specimen, μ shear modulus on the plane shown in Figure 2.2, w out-of-plane specimen width, h half specimen thickness, L half of the span length, and κ the correction factor for shear deformation [17]. Note that in ref. [16], a_1 and a_2 in the above equations are defined as physical crack lengths in the specimen.

The approach used in ref. [16] to derive Eqns. (2.1-2.3) has ignored normal force in the longitudinal direction and bending moment on cross sections at points A and D in Fig. 2.2. As a result, the overhanging sections, i.e. sections KA and DE, were assumed to be load-free. This is incorrect for INF specimen, as evident from Figure 2.4 of a finite element simulation result that shows change in radius of curvature around the right support, suggesting the existence of load on the cross section around the right crack tip that is located on the right of right support.

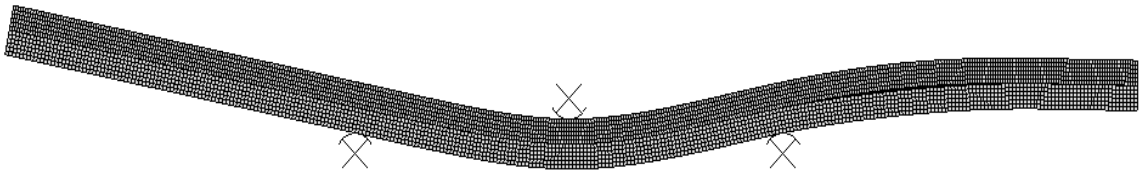

Figure 2.4. Deformation of finite element model of INF specimen

Therefore, this chapter details a revised derivation for specimen compliance and energy release rate, by considering load in the overhanging sections. The close-form expression of the compliance is derived based on Timoshenko beam theory and the energy release rate by the compliance method based on linear elastic fracture mechanics. Both the compliance method and the Timoshenko beam theory will be briefly reviewed in this chapter.

2.2 Compliance method

The energy release rate (G) for any structural configuration can be determined for a given load (P) using the compliance method, which links the change in compliance (dC) due to the change in crack length (da) to the energy release rate, based on linear elastic fracture mechanics, i.e, ($G = \frac{P^2}{2w}\frac{dC}{da}$), where w is the planar crack width.

The key step to use the compliance method is to obtain the expression of C as a function of a. In the following sections, the compliance expression for the INF specimen and energy release rate for delamination will be derived based on Timoshenko beam theory and compliance method, respectively. A brief review of Timoshenko beam theory is discussed in the following sub-section.

2.2.1 The Timoshenko Beam Theory

The Euler-Bernoulli beam theory neglects shear deformations by assuming that plane section remains plane and perpendicular to the neutral axis during bending. However, in reality internal shear stresses develop when a beam is subjected to a transverse load. These stresses cause sections that are perpendicular to the neutral axis of the beam to generate transverse shear deformation on the cross-section. Instead of assuming that the cross-section remains perpendicular to the neutral axis, Timoshenko beam theory assumes that shear strain is uniform on the cross-section and hence, increasing the rotation angle of the cross section, as shown by the combination of ψ and γ in Figure 2.4. The following assumptions are common for both beam theories:

Beam deformation is relatively small

1) The beam is long and slender, i.e. the length is much greater than the width and thickness;

The cross-section of the beam remains plane

2) The beam is made of isotropic, linear elastic material

In the subsequent sections, kinematic and constitutive relationships for the Timoshenko beam theory are used to derive energy release rate and compliance of the INF specimen.

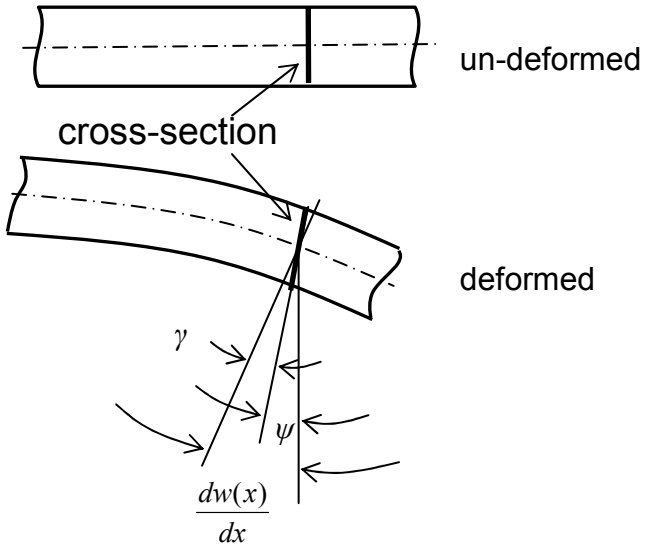

Figure 2.4 Deformation of Timoshenko beam.

2.2.2 The Energy Release Rate for INF Test.

Derivation of the energy release rate has the same approach as that described in ref. [16]. However, instead of ignoring load in the overhanging sections, as adopted for the work on CNF test [15], the derivation takes into account the load in the overhanging sections. The assumptions and derivation of the compliance for the INF specimen is

presented here. The INF specimen is divided into two halves, with the assumption that each half carrying the same amount bending moment, which is equivalent to half of the transverse load for a slender beam, as shown in Figures 2.5(a) and (c). As a result, each diagram in Figures 2.5(a) and (c) contains half of the total transverse load at a given cross section.

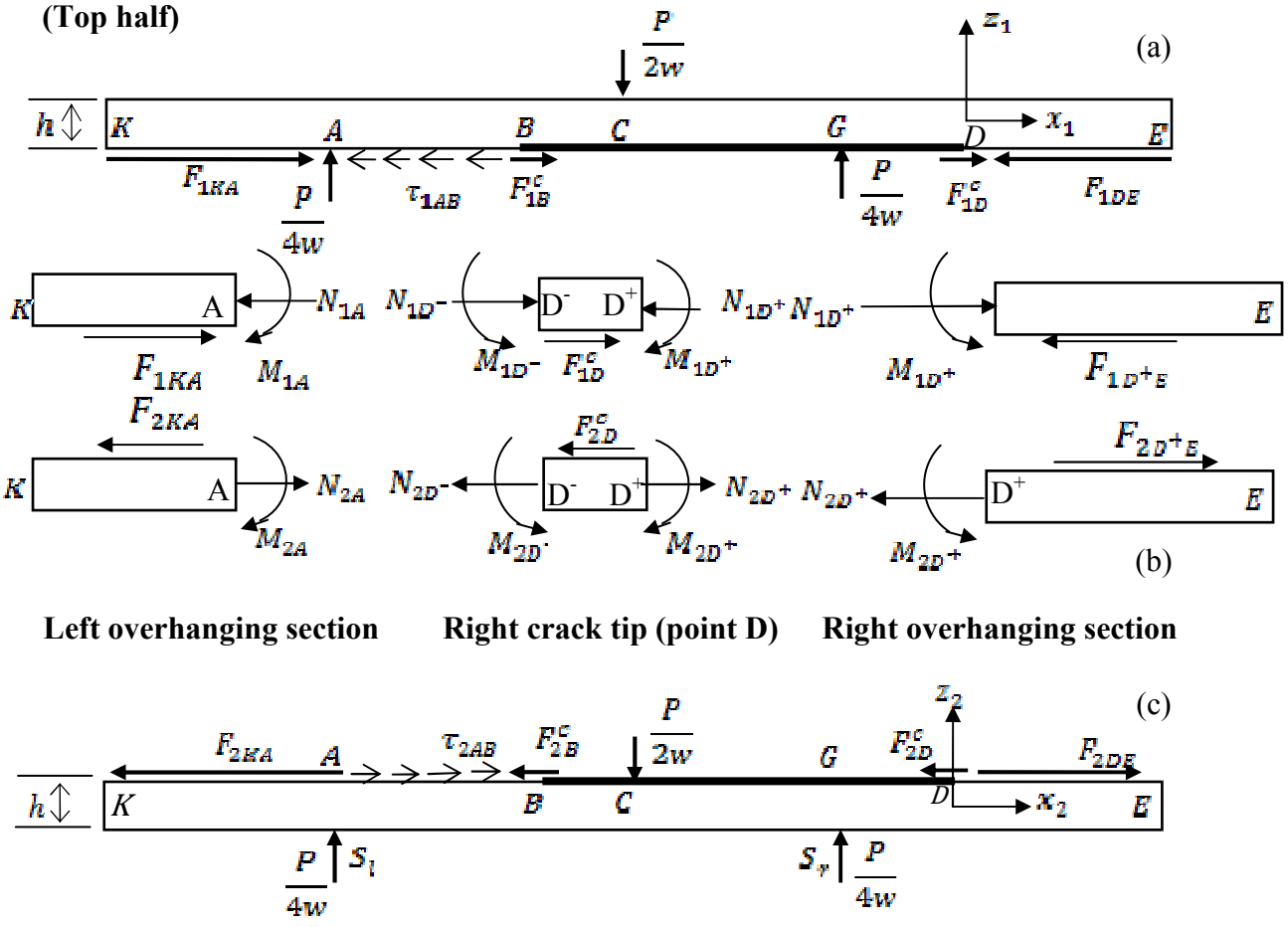

Figure 2.5 Schematic diagrams of load distribution in INF specimen: (a) top half, (b) free body diagrams of left hanging section, right crack tip and right overhanging section, and (c) bottom half.

Expressions for displacement u in the longitudinal direction and deflection δ in the transverse direction for the top and bottom halves of the specimen are given below:

$$u_i(x_i, z_i) = u_i^0 + z_i\psi_i(x_i) \tag{2.4}$$

$$\delta_i = \delta_i(x_i) \tag{2.5}$$

where subscript i is 1 or 2, standing for top or bottom half of the specimen, respectively; coordinates x_i-z_i have the origin located at mid-thickness in each half of the specimen, at a cross section where the right crack tip D is located, as shown in Figure 2.5; $u_i(x_i, z_i)$, u_i^0, $\psi_i(x_i)$, and $\delta_i(x_i)$ are displacement in the x_i-direction at point (x_i, z_i), displacement in the x_i-direction at $z_i = 0$ (mid-plane of the half specimen), the angular displacement of the cross section at x_i, and the vertical deflection at x_i, respectively.

Loading for each half of the specimen is depicted in Figures 2.5(a) and 2.5(c) for the top and bottom half of the specimen, respectively, and Figure 2.5(b) gives free-body diagrams of left and right overhanging sections and the section at right crack tip. Note that in Figure 2.5, F_{iB}^c at point B and F_{iD}^c at point D represent a concentrated shear force at the crack tip, F_{iKA} and F_{iDE} the interlaminar shear force in the overhanging sections *KA* and *DE*, respectively, and τ_{iAB} the distributed interlaminar shear stress in section AB.

Each half of the specimen in Figures 2.5(a) and 2.5(c) is divided into four sections by cross-sections at points *A*, *B*, and *D*. Section *BD* is further divided into three subsections by cross sections at points *C* and *G*.

Load balance in each section is governed by the following equations [15]:

$$\frac{dM_i}{dx} - Q_i + \tau_i(h/2) = 0 \tag{2.6}$$

$$\frac{dQ_i}{dx} = 0 \tag{2.7}$$

$$\frac{dN_i}{dx} + \tau_i = 0 \tag{2.8}$$

where M_i, Q_i, N_i and τ_i are bending moment, transverse force, normal force, and distributed shear stress, respectively, in each half specimen i with unit width (i.e. $w = 1$),

With strain considered to be a first-order function of displacement, the following expressions represent constitutive equations between load and displacement for each half of the specimen.

$$N_i = E\, h \frac{du_i^0}{dx} \tag{2.9}$$

$$M_i = E\, \frac{h^3}{12} \psi_i'(x) \tag{2.10}$$

$$Q_i = \kappa\, \mu\, h \left(\frac{d\delta_i}{dx} + \psi_i \right) \tag{2.11}$$

where h is half of specimen thickness.

In view of the displacement continuity, the following condition should be satisfied between the two halves of the specimen.

$$u_1(x_1, -h/2) = u_2(x_2, h/2) \tag{2.12}$$

Rigid body motion of the specimen can be removed by setting

$$u_{2,S_l} = 0, \text{ and } \delta_{2,S_l} = \delta_{2,S_r} = 0 \tag{2.13}$$

where S_l and S_r are points of support on the left and right, as shown in Figure 2.6.

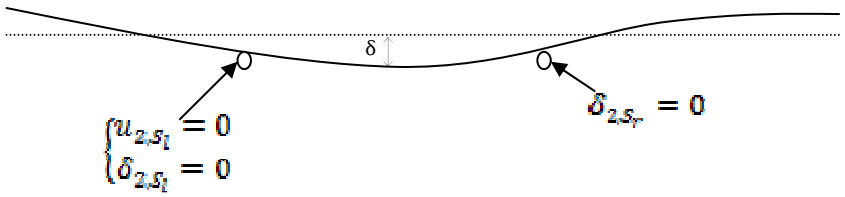

Figure 2.6 Boundary conditions and beam deflection profile

Analytical expression for specimen compliance can be derived using the above equations and boundary conditions, similar to that given in ref. [16]. The main difference

between the two derivations is the consideration of load in the overhanging sections, i.e. load in sections *KA* and *DE* in Figure 2.2. In the previous derivation [16], because loading in those sections was ignored cross section at point *A* was assumed to be load-free and cross section at point *D* free from normal force. In the current derivation, however, shear forces in the interlaminar region of the overhanging sections are considered. Therefore, normal force and bending moment are considered to exist on cross sections at points *A* and *D*.

The key step in the current derivation is to solve for deflection δ from Eqns. (2.6-2.11) for each half of the specimen, with loading specified in Figures 2.5(a) and 2.5(c) and displacement continuity for $\psi(x_i)$, $\delta(x_i)$, and $u^0(x_i)$ across adjacent sections among *KA*, *AB*, *BD*, and *DE*. Solutions from each half specimen are then correlated with each other through displacement continuity between the two halves of the specimen, Eqn. (2.12), with boundary conditions for bottom half of the specimen given by Eqn. (2.13).

Since boundary conditions in Eqn. (2.13) are for the lower half of the specimen, linear displacements, δ and u^0, and angular displacement of the cross section, ψ, for the bottom half of the specimen are solved first. Below are their expressions in terms of x_2.

1) Section AB : $-(a_1+L) \le x_2 \le -(a_1+a_2)$

$$\psi_{2AB}(x_2) = -\frac{3P}{8Eh^3w}[x_2^2 + 2(L+a_1)x_2] + \frac{6N_{2A}}{Eh^2}x_2 - \frac{3P}{8Eh^3wL}(a_2^3 - 3a_2L^2 + a_1^2L + 2a_1L^2 - L^3) - \frac{3N_{2D^-}}{2Eh^2L}(a_2+L)^2 + \frac{3N_{2A}}{2Eh^2L}[(a_2+L)^2 + 4a_1L] \quad (2.14a)$$

$$\delta_{2AB}(x_2) = \frac{P}{8Eh^3w}(x_2^3 + 3(L+a_1)x_2^2 - 2(a_1+L)^3) - \frac{3N_{2A}}{Eh^2}(x_2^2 - (a_1+L)^2) - \left(-\frac{3P}{8Eh^3wL}(a_2^3 - 3a_2L^2 + a_1^2L + 2a_1L^2 - L^3) - \frac{3N_{2C}}{2Eh^2L}(a_2+L)^2 + \frac{3N_{2A}}{2Eh^2L}((a_2+L)^2 + 4a_1L)\right)(x_2 + a_1 + L) - \frac{P}{4\kappa\mu hw}(x_2 + a_1 + L) \quad (2.14b)$$

$$u^0_{2AB}(x_2) = \frac{1}{Eh}\left(\frac{3P}{16wh}[x_2^2 + 2(L+a_1)x_2 + 2(a_1+L)^2] - N_{2A}[x_2 + 4(a_1+L)] + \left(\frac{Eh^2}{2}\right)\left[-\frac{3P}{8Eh^3wL}(\mathrm{a}_2^3 - 3\mathrm{a}_2\mathrm{L}^2 + a_1^2L + 2\mathrm{a}_1\mathrm{L}^2 - \mathrm{L}^3) - \frac{3N_{2C}}{2Eh^2L}(\mathrm{a}_2 + L)^2 + \frac{3N_{2A}}{2Eh^2L}((\mathrm{a}_2 + L)^2 + 4\mathrm{a}_1\mathrm{L})\right]\right) \quad (2.14c)$$

2) Section BC: $-(a_1 + a_2) \le x_2 \le -a_1$

$$\psi_{2BC}(x_2) = -\frac{3P}{8Eh^3w}\left(4x_2^2 + 8(L+a_1)x_2 + 3(a_1+a_2)(a_1-a_2+2L)\right) + \frac{6N_{2C}}{Eh^2}(x_2 + a_1 + a_2) - \frac{6N_{2A}}{Eh^2}(a_1+a_2) - \frac{3P}{8Eh^3wL}(a_2^3 - 3a_2L^2 + a_1^2L + 2a_1L^2 - L^3) - \frac{3N_{2C}}{2Eh^2L}(a_2+L)^2 + \frac{3N_{2A}}{2Eh^2L}((a_2+L)^2 + 4a_1L) \quad (2.15a)$$

$$\delta_{2BC}(x_2) = \frac{P}{8Eh^3w}(4x_2^3 + 12(L+a_1)x_2^2 + 9(a_1+a_2)(a_1-a_2+2L)x_2 + 3(a_1+a_2)^2(3L+a_1-2a_2) - 2(a_1+L)^3) - \frac{3N_{2D^-}}{Eh^2}(x_2^2 + 2(a_1+a_2)x + (a_1+a_2)^2) + \frac{3N_{2A}}{Eh^2}(2(a_1+a_2)x_2 + (a_1+a_2)^2 + (a_1+L)^2) - \left(-\frac{3P}{8Eh^3wL}(a_2^3 - 3a_2L^2 + a_1^2L + 2a_1L^2 - L^3) - \frac{3N_{2D^-}}{2Eh^2L}(a_2+L)^2 + \frac{3N_{2A}}{2Eh^2L}((a_2+L)^2 + 4a_1L)\right)(x_2 + L + a_1) - \frac{P}{4\kappa\mu hw}(x_2 + L + a_1) \quad (2.15b)$$

$$u^0_{2BC} = \frac{1}{Eh}\left(N_{2D^-}(x_2 + a_1 + a_2) + \frac{3P}{16wh}(-(a_1+a_2)(a_1-a_2+2L) + 2(a_1+L)^2) + N_{2A}(-3a_1 + a_2 - 4L) - \frac{3P}{16whL}\left((a_2^3 - 3a_2L^2 + a_1^2L + 2a_1L^2 - L^3)\right) - \frac{3N_{2D^-}}{4L}(a_2 + L)^2 + \frac{3N_{2A}}{4L}((a_2+L)^2 + 4a_1L)\right) \quad (2.15c)$$

3) Section *CG*: $-a_1 \le x_2 \le (-a_1 + L)$

$$\psi_{2CG}(x_2) = \frac{3P}{8Eh^3w}(4x_2^2 + 8(-L + a_1)x_2 + 5a_1^2 + 3a_2^2 - 6a_1L - 6a_2L) + \frac{6N_{2D^-}}{Eh^2}(x_2 + a_1 + a_2) - \frac{6N_{2A}}{Eh^2}(a_1 + a_2) - \frac{3P}{8Eh^3wL}(a_2^3 - 3a_2L^2 + a_1^2L + 2a_1L^2 - L^3) - \frac{3N_{2D^-}}{2Eh^2L}((a_2 + L)^2) + \frac{3N_{2A}}{2Eh^2L}((a_2 + L)^2 + 4a_1L) \quad (2.16a)$$

$$\delta_{2CG}(x_2) = \frac{P}{8Eh^3w}(-4x_2^3 - 12(-L + a_1)x_2^2 - 3(5a_1^2 + 3a_2^2 - 6a_1L - 6a_2L)x_2 - 7a_1^3 - 9a_1a_2^2 + 18a_1a_2L - 6a_2^3 + 9a_2^2L + 3a_1^2L - 6a_1L^2 - 2L^3) - \frac{3N_{2D^-}}{Eh^2}(x_2^2 + 2(a_1 + a_2)x_2 + (a_1 + a_2)^2) + \frac{3N_{2A}}{Eh^2}(2(a_1 + a_2)x_2 + (a_1 + a_2)^2 + (a_1 + L)^2) - \left(-\frac{3P}{8Eh^3wL}\left((a_2^3 - 3a_2L^2 + a_1^2L + 2a_1L^2 - L^3)\right) - \frac{3N_{2D^-}}{2Eh^2L}((a_2 + L)^2) + \frac{3N_{2A}}{2Eh^2L}((a_2 + L)^2 + 4a_1L)\right)(x_2 + L + a_1) - \frac{P}{4\kappa\mu hw}(L - x_2 - a_1) \quad (2.16b)$$

$$u_{2CG}^0 = \frac{1}{Eh}\left(N_{2D^-}(x_2 + a_1 + a_2) + \frac{3P}{16wh}(-(a_1 + a_2)(a_1 - a_2 + 2L) + 2(a_1 + L)^2) + N_{2A}(-3a_1 + a_2 - 4L) - \frac{3P}{16whL}\left((a_2^3 - 3a_2L^2 + a_1^2L + 2a_1L^2 - L^3)\right) - \frac{3N_{2D^-}}{4L}(a_2 + L)^2 + \frac{3N_{2A}}{4L}((a_2 + L)^2 + 4a_1L)\right) \quad (2.16c)$$

4) Section *GD*: $(-a_1 + L) \le x_2 \le 0$

$$\psi_{2GD}(x_2) = \frac{3N_{2D^-}}{2Eh^2L}(4Lx_2 - (a_2 - L)^2 + 4La_1) + \frac{3P}{8Eh^3wL}(3a_2^2L - 3a_2L^2 - 3L^3 - a_2^3) + \frac{3N_{2A}}{2Eh^2L}((a_2 - L)^2) \quad (2.17a)$$

$$\delta_{2GD}(x_2) = \frac{3N_{2D^-}}{2Eh^2L}\left(-2Lx_2^2 + (a_2 - L)^2x_2 - 4La_1x_2 + 2L(-a_1 + L)^2 - (a_2 - L)^2(-a_1 + L) + 4La_1(-a_1 + L)\right) - \frac{3P}{8Eh^3wL}\left((3a_2^2L - 3a_2L^2 - 3L^3 - a_2^3)x_2 - (3a_2^2L - 3a_2L^2 - 3L^3 - a_2^3)(-a_1 + L)\right) - \frac{3N_{2A}}{2Eh^2L}\left((a_2 - L)^2x_2 - (a_2 - L)^2(-a_1 + L)\right) \quad (2.17b)$$

$$u^0_{2GD} = \frac{1}{Eh}\Big(N_{2D^-}(x_2 + a_1 + a_2) + \frac{3P}{16wh}[-(a_1 + a_2)(a_1 - a_2 + 2L) + 2(a_1 + L)^2] + N_{2A}(-3a_1 + a_2 - 4L) - \frac{3P}{16whL}\big((a_2^3 - 3a_2L^2 + a_1^2L + 2a_1L^2 - L^3)\big) - \frac{3N_{2D^-}}{4L}(a_2 + L)^2 + \frac{3N_{2A}}{4L}[(a_2 + L)^2 + 4a_1L]\Big) \quad (2.17c)$$

5) Section DE: $0 \le x_2 \le l_r$, where l_r is length of un-delaminated region in the right overhanging section of the specimen

$$\psi_{2DE}(x_2) = -\frac{6N_{2D^+}}{Eh^2}\Big(\frac{x^2}{2l_r} - x_2\Big) + \frac{3N_{2D^-}}{2Eh^2L}(-(a_2 - L)^2 + 4La_1) + \frac{3P}{8Eh^3wL}(3a_2^2L - 3a_2L^2 - 3L^3 - a_2^3) + \frac{3N_{2A}}{2Eh^2L}(a_2 - L)^2 \quad (2.18a)$$

$$\delta_{2DE}(x_2) = -\Big(-\frac{6N_{2D^+}}{Eh^2}\Big(\frac{x^3}{6l_r} - \frac{1}{2}x_2^2\Big) + \Big(\frac{3N_{2D^-}}{2Eh^2L}(-(a_2 - L)^2 + 4La_1) + \frac{3P}{8Eh^3wL}(3a_2^2L - 3a_2L^2 - 3L^3 - a_2^3) + \frac{3N_{2A}}{2Eh^2L}((a_2 - L)^2)\Big)x_2\Big) + \frac{3N_{2D^-}}{2Eh^2L}\big(2L(-a_1 + L)^2 - (a_2 - L)^2(-a_1 + L) + 4La_1(-a_1 + L)\big) - \frac{3P}{8Eh^3wL}\big(-(3a_2^2L - 3a_2L^2 - 3L^3 - a_2^3)(-a_1 + L)\big) - \frac{3N_{2A}}{2Eh^2L}\big(-(a_2 - L)^2(-a_1 + L)\big) \quad (2.18b)$$

$$u^0_{2DE}(x_2) = \frac{1}{Eh}\Big(N_{2D^+}\Big(\frac{x_2^2}{2l_r} - x\Big) + N_{2D^-}(a_1 + a_2) + \frac{3P}{16wh}(-(a_1 + a_2)(2L + a_1 - a_2) + 2(a_1 + L)^2) + N_{2A}(-3a_1 - a_2 - 2L) - \frac{3P}{16whL}(a_2^3 - 3a_2L^2 + a_1^2L + 2a_1L^2 - L^3) - \frac{3N_{2D^-}}{4L}(a_2 + L)^2 + \frac{3N_{2A}}{4L}((a_2 + L)^2 + 4a_1L)\Big) \quad (2.18c)$$

In a similar manner, expressions for deflection, $\delta(x_1)$, angular displacement of the cross-section, $\psi(x_1)$, and displacement along neutral axis, $u^0(x_1)$, of various sections in the upper half of the specimen are:

1) Section AB: $-(a_1 + L) \le x_1 \le -(a_1 + a_2)$

$$\psi_{1AB}(x_1) = -\frac{3P}{8Eh^3w}(x_1^2 + 2(L+a_1)x_1) + \frac{6N_{1A}}{Eh^2}x_1 - \frac{3P}{8Eh^3wL}(a_2^3 - 3a_2L^2 + a_1^2L + 2a_1L^2 - L^3) - \frac{3N_{1D^-}}{2Eh^2L}(a_2+L)^2 + \frac{3N_{1A}}{2Eh^2L}((a_2+L)^2 + 4a_1L) \quad (2.19a)$$

$$\delta_{1AB}(x_1) = \frac{P}{8Eh^3w}(x_1^3 + 3(L+a_1)x_1^2 - 2(a_1+L)^3) - \frac{3N_{1A}}{Eh^2}(x_1^2 - (a_1+L)^2) - \left(-\frac{3P}{8Eh^3wL}(a_2^3 - 3a_2L^2 + a_1^2L + 2a_1L^2 - L^3) - \frac{3N_{1D^-}}{2Eh^2L}(a_2+L)^2 + \frac{3N_{1A}}{2Eh^2L}((a_2+L)^2 + 4a_1L)\right)(x_1 + a_1 + L) - \frac{P}{4\kappa\mu hw}(x_1 + a_1 + L) \quad (2.19b)$$

$$u_{1AB}^0(x_1) = \frac{1}{Eh}\left(\frac{3P}{16wh}(x^2 + 2(L+a_1)x + 4(a_1+L)^2) + N_{1A}x - 2N_{1A}(a_1+L) - 6N_{2A}(a_1+L) + -\frac{9P}{16hwL}(a_2^3 - 3a_2L^2 + a_1^2L + 2a_1L^2 - L^3) - \frac{9N_{2D^-}}{4L}(a_2+L)^2 + \frac{9N_{2A}}{4L}((a_2+L)^2 + 4a_1L)\right) \quad (19c)$$

2) Section BC: $-(a_1 + a_2) \le x_1 \le -a_1$

$$\psi_{1BC}(x_1) = -\frac{3P}{8Eh^3w}\left(4x_1^2 + 8(L+a_1)x_1 + 3(a_1+a_2)(a_1-a_2+2L)\right) + \frac{6N_{1C}}{Eh^2}(x_1 + a_1 + a_2) - \frac{6N_{1A}}{Eh^2}(a_1+a_2) - \frac{3P}{8Eh^3wL}(a_2^3 - 3a_2L^2 + a_1^2L + 2a_1L^2 - L^3) - \frac{3N_{2C}}{2Eh^2L}(a_2+L)^2 + \frac{3N_{2A}}{2Eh^2L}((a_2+L)^2 + 4a_1L) \quad (2.20a)$$

$$\delta_{1BC}(x_1) = \frac{P}{8Eh^3w}(4x_1^3 + 12(L+a_1)x_1^2 + 9(a_1+a_2)(a_1-a_2+2L)x_1 + 3(a_1+a_2)^2(3L + a_1 - 2a_2) - 2(a_1+L)^3) - \frac{3N_{1D^-}}{Eh^2}(x_1^2 + 2(a_1+a_2)x_1 + (a_1+a_2)^2) + \frac{3N_{1A}}{Eh^2}(2(a_1+a_2)x_1 + (a_1+a_2)^2 + (a_1+L)^2) - \left(-\frac{3P}{8Eh^3wL}(a_2^3 - 3a_2L^2 + a_1^2L + 2a_1L^2 - L^3) - \frac{3N_{1D^-}}{2Eh^2L}(a_2+L)^2 + \frac{3N_{1A}}{2Eh^2L}((a_2+L)^2 + 4a_1L)\right)(x_1 + L + a_1) - \frac{P}{4\kappa\mu hw}(x_1 + L + a_1) \quad (2.20b)$$

$$u^0_{1BC}(x_1) = \frac{1}{Eh}\Big(-N_{1D^-}(x_1 + a_1 + a_2) + \frac{3P}{16wh}((a_2 - L)^2 + 3(a_1 + L)^2) - N_{1A}(4L + 3a_1 - a_2) - 6N_{1A}(a_1 + L) - \frac{9P}{16whL}(a_2^3 - 3a_2L^2 + a_1^2L + 2a_1L^2 - L^3) - \frac{9N_{1D^-}}{4L}(a_2 + L)^2 + \frac{9N_{1A}}{4L}((a_2 + L)^2 + 4a_1L)\Big) \quad (2.20c)$$

3) Section *CG*: $-a_1 \le x_1 \le (-a_1 + L)$

$$\psi_{1CG}(x_1) = \frac{3P}{8Eh^3w}(4x_1^2 + 8(-L + a_1)x_1 + 5a_1^2 + 3a_2^2 - 6a_1L - 6a_2L) + \frac{6N_{1D^-}}{Eh^2}(x_1 + a_1 + a_2) - \frac{6N_{1A}}{Eh^2}(a_1 + a_2) - \frac{3P}{8Eh^3wL}(a_2^3 - 3a_2L^2 + a_1^2L + 2a_1L^2 - L^3) - \frac{3N_{1D^-}}{2Eh^2L}((a_2 + L)^2) + \frac{3N_{1A}}{2Eh^2L}((a_2 + L)^2 + 4a_1L) \quad (2.21a)$$

$$\delta_{1CG}(x_1) = \frac{P}{8Eh^3w}(-4x_1^3 - 12(-L + a_1)x_1^2 - 3(5a_1^2 + 3a_2^2 - 6a_1L - 6a_2L)x_1 - 7a_1^3 - 9a_1a_2^2 + 18a_1a_2L - 6a_2^3 + 9a_2^2L + 3a_1^2L - 6a_1L^2 - 2L^3) - \frac{3N_{1D^-}}{Eh^2}(x_1^2 + 2(a_1 + a_2)x_1 + (a_1 + a_2)^2) + \frac{3N_{1A}}{Eh^2}(2(a_1 + a_2)x_1 + (a_1 + a_2)^2 + (a_1 + L)^2) - \Big(-\frac{3P}{8Eh^3wL}\big((a_2^3 - 3a_2L^2 + a_1^2L + 2a_1L^2 - L^3)\big) - \frac{3N_{1D^-}}{2Eh^2L}((a_2 + L)^2) + \frac{3N_{1A}}{2Eh^2L}((a_2 + L)^2 + 4a_1L)\Big)(x_1 + L + a_1) - \frac{P}{4\kappa\mu hw}(L - x_1 - a_1) \quad (2.21b)$$

$$u^0_{1CG}(x_1) = \frac{1}{Eh}\Big(-N_{1D^-}(x_1 + a_1 + a_2) + \frac{3P}{16wh}((a_2 - L)^2 + 3(a_1 + L)^2) - N_{1A}(4L + 3a_1 - a_2) - 6N_{1A}(a_1 + L) - \frac{9P}{16whL}(a_2^3 - 3a_2L^2 + a_1^2L + 2a_1L^2 - L^3) - \frac{9N_{1D^-}}{4L}(a_2 + L)^2 + \frac{9N_{1A}}{4L}((a_2 + L)^2 + 4a_1L)\Big) \quad (2.21c)$$

4) Section *GD*: $(-a_1 + L) \le x_1 \le 0$,

$$\psi_{1GD}(x_1) = \frac{6N_{1D^-}}{Eh^2}(x_1 + a_1 + a_2) + \frac{3P}{8Eh^3w}(a_1^2 + 3a_2^2 + 2a_1L - 6a_2L - 4L^2) - \frac{6N_{1A}}{Eh^2}(a_1 + a_2) - \frac{3P}{8Eh^3wL}(a_2^3 - 3a_2L^2 + a_1^2L + 2a_1L^2 - L^3) - \frac{3N_{1D^-}}{2Eh^2L}(a_2 + L)^2 + \frac{3N_{1A}}{2Eh^2L}((a_2 + L)^2 + 4a_1L) \quad (2.22a)$$

$$\delta_{1GD}(x_1) = \frac{3N_{1D^-}}{2Eh^2L}\left(-2Lx_1^2 + (a_2 - L)^2x_1 - 4La_1x_1 + 2L(-a_1 + L)^2 - (a_2 - L)^2(-a_1 + L) + 4La_1(-a_1 + L)\right) - \frac{3P}{8Eh^3wL}\left((3a_2^2L - 3a_2L^2 - 3L^3 - a_2^3)x_1 - (3a_2^2L - 3a_2L^2 - 3L^3 - a_2^3)(-a_1 + L)\right) - \frac{3N_{1A}}{2Eh^2L}\left((a_2 - L)^2x_1 - (a_2 - L)^2(-a_1 + L)\right) \quad (2.22b)$$

$$u_{1GD}^0(x_1) = \frac{1}{Eh}\left(-N_{1D^-}(x_1 + a_1 + a_2) - \frac{3P}{16wh}\left((a_1 + a_2)(2L + a_1 - a_2)\right) + \frac{3P}{4wh}(a_1 + L)^2 + N_{1A}(-3a_1 - a_2 - 2L) - 6N_{2A}(a_1 + L) - \frac{9P}{16whL}(a_2^3 - 3a_2L^2 + a_1^2L + 2a_1L^2 - L^3) - \frac{9N_{1D^-}}{4L}(a_2 + L)^2 + \frac{9N_{1A}}{4L}((a_2 + L)^2 + 4a_1L)\right) \quad (2.22c)$$

5) Section DE: $0 \le x_1 \le l_r$, where l_r length of undelaminated region in the right overhanging section of the specimen

$$\psi_{1D^+E}(x_1) = -\frac{6N_{1D^+}}{Eh^2}\left(\frac{x_1^2}{2l_r} - x_1\right) + \frac{3N_{2D^-}}{2Eh^2L}(-(a_2 - L)^2 + 4La_1) + \frac{3P}{8Eh^3wL}(3a_2^2L - 3a_2L^2 - 3L^3 - a_2^3) + \frac{3N_{2A}}{2Eh^2L}((a_2 - L)^2) \quad (2.23a)$$

$$\delta_{1DE}(x_1) = -\left(-\frac{6N_{1D^+}}{Eh^2}\left(\frac{x_1^3}{6l_r} - \frac{1}{2}x_1^2\right) + \left(\frac{3N_{2D^+}}{2Eh^2L}(-(a_2 - L)^2 + 4La_1) + \frac{3P}{8Eh^3wL}(3a_2^2L - 3a_2L^2 - 3L^3 - a_2^3) + \frac{3N_{2A}}{2Eh^2L}((a_2 - L)^2)\right)x_1\right) + \frac{3N_{2D^-}}{2Eh^2L}\left(2L(-a_1 + L)^2 - (a_2 - L)^2(-a_1 + L) + 4La_1(-a_1 + L)\right) - \frac{3P}{8Eh^3wL}\left(-(3a_2^2L - 3a_2L^2 - 3L^3 - a_2^3)(-a_1 + L)\right) - \frac{3N_{2A}}{2Eh^2L}\left(-(a_2 - L)^2(-a_1 + L)\right) \quad (2.23b)$$

$$u^0_{1DE}(x_1) = \frac{1}{Eh}\left(N_{1D^+}\left(\frac{x_1^2}{2l_r} - x_1\right) - N_{1D}(a_1 + a_2) + \frac{3P}{16wh}((a_2 - L)^2 + 3(a_1 + L)^2) - N_{1A}(4L + 3a_1 - a_2) - 6N_{2A}(a_1 + L) + \left(\frac{3Eh^2}{2}\right)\left(\frac{P}{8Eh^3wL}(-3(a_2^3 - 3a_2L^2 + a_1^2L + 2a_1L^2 - L^3)) - \frac{3N_{2D^-}}{2Eh^2L}(a_2 + L)^2 + \frac{3N_{2A}}{2Eh^2L}((a_2 + L)^2 + 4a_1L)\right)\right) \quad (2.23c)$$

On cross sections at points B,D and E in Figure 2.2, expressions for $u^0$and ψ for each half of the specimen are:

(i) In the top half of the specimen:

$$u^0_{1AB}(-a_1 - a_2) = \frac{1}{Eh}\left(\frac{3P}{16wh}((a_2 - L)^2 + 3(a_1 + L)^2) + N_{1A}(-3a_1 - a_2 - 2L) - 6N_{1A}(a_1 + L) + -\frac{9P}{16hwL}(a_2^3 - 3a_2L^2 + a_1^2L + 2a_1L^2 - L^3) - \frac{9N_{2D^-}}{4L}(a_2 + L)^2 + \frac{9N_{1A}}{4L}((a_2 + L)^2 + 4a_1L)\right) \quad (2.24a)$$

$$u^0_{1GD}(0) = \frac{1}{Eh}\left(-N_{1D^-}(a_1 + a_2) - \frac{3P}{16wh}\left((a_1 + a_2)(2L + a_1 - a_2)\right) + \frac{3P}{4wh}(a_1 + L)^2 - N_{1A}(3a_1 + a_2 + 2L) - 6N_{2A}(a_1 + L) - \frac{9P}{16whL}(a_2^3 - 3a_2L^2 + a_1^2L + 2a_1L^2 - L^3) - \frac{9N_{1D^-}}{4L}(a_2 + L)^2 + \frac{9N_{1A}}{4L}((a_2 + L)^2 + 4a_1L)\right) \quad (2.24b)$$

$$u^0_{1DE}(l_r) = \frac{1}{Eh}\left(N_{1D^+}\left(\frac{{l_r}^2}{2l_r} - l_r\right) - N_{1D^-}(a_1 + a_2) + \frac{3P}{16wh}((a_2 - L)^2 + 3(a_1 + L)^2) - N_{1A}(4L + 3a_1 - a_2) - 6N_{1A}(a_1 + L) + \frac{3P}{16hwL}(-3(a_2^3 - 3a_2L^2 + a_1^2L + 2a_1L^2 - L^3)) - \frac{9N_{2D^-}}{4L}((a_2 + L)^2) + \frac{9N_{1A}}{4L}((a_2 + L)^2 + 4a_1L)\right) \quad (2.24c)$$

$$\psi_{1AB}(-a_1 - a_2) = \frac{3P}{8Eh^3w}\left((a_1 + a_2)(2L + a_1 - a_2)\right) - \frac{6N_{1A}}{Eh^2}(a_1 + a_2) - \frac{3P}{8Eh^3wL}(a_2^3 - 3a_2L^2 + a_1^2L + 2a_1L^2 - L^3) - \frac{3N_{1D^-}}{2Eh^2L}(a_2 + L)^2 + \frac{3N_{1A}}{2Eh^2L}((a_2 + L)^2 + 4a_1L) \quad (2.24d)$$

$$\psi_{1GD}(0) = \frac{6N_{1D^-}}{Eh^2}(a_1 + a_2) + \frac{3P}{8Eh^3w}(a_1^2 + 3a_2^2 + 2a_1L - 6a_2L - 4L^2) - \frac{6N_{1A}}{Eh^2}(a_1 + a_2) - \frac{3P}{8Eh^3wL}\left((a_2^3 - 3a_2L^2 + a_1^2L + 2a_1L^2 - L^3)\right) - \frac{3N_{1D^-}}{2Eh^2L}((a_2 + L)^2) + \frac{3N_{1A}}{2Eh^2L}((a_2 + L)^2 + 4a_1L) \quad (2.24e)$$

$$\psi_{1DE}(l_r) = \frac{3l_rN_{1D^+}}{Eh^2} + \frac{3N_{1D^-}}{2Eh^2L}(-(a_2 - L)^2 + 4La_1) + \frac{3P}{8Eh^3wL}(3a_2^2L - 3a_2L^2 - 3L^3 - a_2^3) + \frac{3N_{1A}}{2Eh^2L}(a_2 - L)^2 \quad (2.24f)$$

(ii) In the bottom half of the specimen

$$u^0_{2AB}(-a_1 - a_2) = \frac{1}{Eh}\left(\frac{3P}{16wh}(-(a_1 + a_2)(a_1 - a_2 + 2L) + 2(a_1 + L)^2) + N_{2A}\left((-3a_1 + a_2 - 4L)\right) - \frac{3P}{16hwL}(a_2^3 - 3a_2L^2 + a_1^2L + 2a_1L^2 - L^3) - \frac{3N_{2D^-}}{4L}(a_2 + L)^2 + \frac{3N_{2A}}{2L}((a_2 + L)^2 + 4a_1L)\right) \quad (2.25a)$$

$$u^0_{2GD}(0) = \frac{1}{Eh}\left(N_{2D^-}(a_1 + a_2) + \frac{3P}{16wh}(-(a_1 + a_2)(a_1 - a_2 + 2L) + 2(a_1 + L)^2) + N_{2A}(-3a_1 + a_2 - 4L) - \frac{3P}{16whL}(a_2^3 - 3a_2L^2 + a_1^2L + 2a_1L^2 - L^3) - \frac{3N_{2D^-}}{4L}(a_2 + L)^2 + \frac{3N_{2A}}{4L}((a_2 + L)^2 + 4a_1L)\right) \quad (2.25b)$$

$$u^0_{2DE}(l_r) = \frac{1}{Eh}\left(-\frac{l_r N_{2D^+}}{2} + N_{2D^-}(a_1 + a_2) + \frac{3P}{16wh}(-(a_1 + a_2)(2L + a_1 - a_2) + 2(a_1 + L)^2) + N_{2A}(-3a_1 - a_2 - 2L) - \frac{3P}{16whL}(a_2^3 - 3a_2L^2 + a_1^2L + 2a_1L^2 - L^3) - \frac{3N_{2D^-}}{4L}(a_2 + L)^2 + \frac{3N_{2A}}{4L}((a_2 + L)^2 + 4a_1L)\right) \quad (2.25c)$$

$$\psi_{2AB}(-a_1 - a_2) = \frac{3P}{8Eh^3w}(a_1 + a_2)(a_1 - a_2 + 2L) - \frac{6N_{2A}}{Eh^2}(a_1 + a_2) - \frac{3P}{8Eh^3w^2L}(a_2^3 - 3a_2L^2 + a_1^2L + 2a_1L^2 - L^3) - \frac{3N_{2D^-}}{2Eh^2L}(a_2 + L)^2 + \frac{3N_{2A}}{2Eh^2L}((a_2 + L)^2 + 4a_1L) \quad (2.25d)$$

$$\psi_{2GD}(0) = \frac{6N_{2D^-}}{Eh^2}(a_1 + a_2) + \frac{3P}{8Eh^3w}(a_1^2 + 3a_2^2 + 2a_1L - 6a_2L - 4L^2) - \frac{6N_{2A}}{Eh^2}(a_1 + a_2) - \frac{3P}{8Eh^3wL}(a_2^3 - 3a_2L^2 + a_1^2L + 2a_1L^2 - L^3) - \frac{3N_{2D^-}}{2Eh^2L}(a_2 + L)^2 + \frac{3N_{2A}}{2Eh^2L}((a_2 + L)^2 + 4a_1L) \quad (2.25e)$$

$$\psi_{2DE}(l_r) = \frac{3l_r N_{2D^+}}{Eh^2} + \frac{3N_{2D^-}}{2Eh^2L}(-(a_2 - L)^2 + 4La_1) + \frac{3P}{8Eh^3wL}(3a_2^2L - 3a_2L^2 - 3L^3 - a_2^3) + \frac{3N_{2A}}{2Eh^2L}(a_2 - L)^2 \quad (2.25f)$$

Boundary conditions selected here are given as in the following expressions. The first two are to set displacement u_i at the left and right crack tips to be the same between the top and bottom halves of the specimen, which is the relaxed version of the assumption made by Maikumar et al. [15]. The third boundary condition, in view that the crack only grows from the right crack tip, is to set displacement u_i at point A, the interlaminar point above the left support, to be the same between the top and bottom halves of the specimen.

$$u_1(-a_1 - a_2, -h/2) = u_2(-a_1 - a_2, h/2) \quad (2.26a)$$

$$u_1(0, -h/2) = u_2(0, h/2) \quad (2.26b)$$

$$u_1(-L - a_1, -h/2) = u_2(-L - a_1, h/2) \quad (2.26c)$$

where expressions for u_1 and u_2 are

$$u_1(-a_1 - a_2, -h/2) = u_{1AB}^0(-a_1 - a_2) - \left(\frac{h}{2}\right)\psi_{1AB}(-a_1 - a_2) \quad (2.27a)$$

$$u_2(-a_1 - a_2, h/2) = u_{2AB}^0(-a_1 - a_2) + \left(\frac{h}{2}\right)\psi_{2AB}(-a_1 - a_2) \quad (2.27b)$$

$$u_1(0, -h/2) = u_{1GD}^0(0) - \left(\frac{h}{2}\right)\psi_{1GD}(0) \quad (2.27c)$$

$$u_2(0, h/2) = u_{2GD}^0(0) + \left(\frac{h}{2}\right)\psi_{2GD}(0) \quad (2.27d)$$

$$u_1(-L - a_1, -h/2) = u_{1AB}^0(-L - a_1) - \left(\frac{h}{2}\right)\psi_{1AB}(-L - a_1) \quad (2.27e)$$

$$u_2(-L-a_2, h/2) = u^0_{2AB}(-L-a_2) + \left(\frac{h}{2}\right)\psi_{2AB}(-L-a_2) \tag{2.27f}$$

Based on expressions given in Eqns. (2.24-2.25), the above boundary conditions can be used to solve for$N_{iA}, N_{iD^-}$and N_{iD^+}. Note that $N_{1A} = N_{2A}$, $N_{1D^-} = N_{2D^-}$ and $N_{1D^+} = N_{2D^+}$ due to symmetry of the loading conditions, as shown by free body diagrams in Figure 2.5(b). This yields

$$N_{iA} = -\frac{3P}{32wh}(L-a_2) \tag{2.28a}$$

$$N_{iD^-} = -\frac{3P}{16wh(a_1+a_2)}(a_2^2 - 2a_2L - L^2) \tag{2.28b}$$

$$N_{iD^+} = -\frac{3P}{32whl_r}(3La_1 + a_2L - 3a_2a_1 - 2a_2^2 + 3L^2) \tag{2.28c}$$

Once the above normal forces are determined, expressions for the concentrated forces, $F^c_{2B}$and F^C_{2D}can be expressed below, based on free body diagrams of the left and right crack tips. Note that the free body diagram for the right crack tip in Figure 2.5(b) can also represent the free body diagram for the left crack tip, by replacing "D" in the diagram by "B." Expressions for the concentrated forces, F^c_{2B} and F^c_{2D}, are

$$F^c_{2B} = \frac{3P}{16wh(a_1+a_2)}\left(a_2^2 + 2a_1a_2 - 2a_1L + L^2 - \frac{1}{2}(a_1+a_2)(L-a_2)\right) \tag{2.29a}$$

$$F^c_{2D} = \frac{3P}{16wh(a_1+a_2)}\left(a_2^2 - 2a_2L - L^2 - \frac{(a_1+a_2)}{2l_r}(3La_1 + a_2L - 3a_2a_1 - 2a_2^2 + 3L^2)\right) \tag{2.29b}$$

If shear force in the interlaminar region of the overhanging section is ignored, the expressions in Eqns. (2.29a) and (2.29b) are reduced to

$$F^c_{2B} = \frac{3P}{16wh(a_1+a_2)}(a_2^2 + 2a_1a_2 - 2a_1L + L^2) \tag{2.30a}$$

$$F^c_{2D} = \frac{3P}{16wh(a_1+a_2)}(a_2^2 - 2a_2L - L^2) \tag{2.30b}$$

By substituting Eqns. (2.28a) and (2.28b) into Eqn. (2.21b), the center deflection of the specimen, $\delta_{1CG}(-a_1)$, is:

$$\delta_{1CG}(-a_1) = -\frac{PL^3}{4Eh^3w} - \frac{PL}{4\kappa\mu hw} - \frac{3P}{8Eh^3w}(a_2^3 - 3a_2^2L + 3a_2L^2 + L^3) + \frac{9P}{32Eh^3w(a_1+a_2)}(a_2^2 - 2a_2L - L^2)^2 + \frac{9P}{64Eh^3w}(a_2 - L)^3 \quad (2.31)$$

Hence, compliance for the specimen C is:

$$C = \frac{1}{2}\left(\frac{\delta_{1CG(-a_1)}}{-P/2}\right) = \frac{L^3}{4Eh^3w} + \frac{L}{4\kappa\mu hw} + \frac{3(-3L^4-8a_2L^3+4a_1L^3+6a_2^2L^2+12a_1a_2L^2-12a_1a_2^2L+4a_1a_2^3+a_2^4)}{32Eh^3w(a_1+a_2)} + \frac{9}{64Eh^3w}(L - a_2)^3 \quad (2.32)$$

In Eqn. (2.32), the fourth term on the right-hand side is due to the consideration of interlaminar shear force in the overhanging section. If ignored, the expression for C is reduced to Eqn. (2.1).

It should be noted that a unidirectional fiber composite beam is transversely isotropic, not isotropic as assumed for the beam theory used here. However, since the deformation is considered to be in the plane-strain condition with modulus in the axial direction affecting the deformation, the beam theory is still applicable as long as the material constants E and μ represent flexural modulus in the longitudinal direction and shear modulus on the longitudinal-thickness plane, respectively. For example, in the case that the local 1-direction of the material is along the longitudinal direction, the material constants E and μ in Eqn. (2.32) represent E_{11} and μ_{12}, respectively.

Based on the compliance method discussed in section 2.2.1 [18], the energy release rate G for delamination growth in directions a_i is

$$G_{a_i} = \frac{P^2}{2w}\frac{\partial C}{\partial a_i} \quad (2.33)$$

That is,

$$G_{a_1} = \frac{9P^2}{64Ew^2h^3(a_1+a_2)^2}[a_2^2 - 2a_2L - L^2]^2 \quad (2.34a)$$

$$G_{a_2} = \frac{9P^2}{64Ew^2h^3(a_1+a_2)^2}\left[(a_2^2 + 2a_1a_2 - 2a_1L + L^2)^2 - \frac{3}{2}(a_1+a_2)^2(L-a_2)^2\right] \quad (2.34b)$$

Note that if the interlaminar shear load in the overhanging sections were ignored, the expressions for G_{ai} would then be reduced to Eqns. (2.2) and (2.3) that were reported in ref. [16].

Now the total energy release rate G for crack growth from the two crack fronts can be expressed as a function of G_{a_1} and G_{a_2}, by incorporating fraction of the delamination growth length in the two directions, i.e.,

$$G = \frac{\Delta a_1}{\Delta a_1+\Delta a_2}G_{a_1} + \frac{\Delta a_2}{\Delta a_1+\Delta a_2}G_{a_2} \quad (2.35)$$

For delamination growth only in a_1-direction, G_{a_1} has to be greater than G_{a_2}, which can be met by enforcing $G_{a_1} > G_{a_2}$ for the initial values of a_1 and a_2. In addition, a_1 should be longer than L. Therefore, the initial values for a_1 and a_2 should meet the following condition [16]:

$$L \le a_1 \le \frac{L + a_2}{L - a_2}L \quad (2.36)$$

When the above condition is met,

$$G = G_{a_1} = \frac{9P^2}{64Ew^2h^3(a_1+a_2)^2}[a_2^2 - 2a_2L - L^2]^2 \quad (2.37)$$

Eqn. (2.36) also suggests that a limit exists for the growth of a_1 before delamination growth starts in a_2-direction. Therefore, dimensions of the INF specimen should be designed to ensure that the specimen provides sufficient growth in a_1-direction before the growth in a_2-direction starts, for ease of establishing the resistance curve for delamination.

2.3 Prediction of Load-Displacement Curve for INF test

In the condition that delamination grows in a_1 direction only, Eqn. (2.37) can be used to construct load-displacement curve for INF test provided that critical energy release rate G_C is constant during the delamination growth. In this case, load P can be expressed as:

$$P = \frac{8(a_1+a_2)\sqrt{Ew^2h^3G_C}}{3(L^2+2a_2L-a_2^2)} \tag{2.38}$$

The corresponding expression for the displacement δ is

$$\delta = \frac{\sqrt{G_C}(-9L^4-16a_2L^3+20a_1L^3+18a_2^2L^2+36a_1a_2L^2-36a_1a_2^2L+12a_1a_2^3+3a_2^4)}{12\sqrt{Eh^3}(L^2+2a_2L-a_2^2)} + \frac{9\sqrt{G_C}(a_1+a_2)(L-a_2)^3}{24\sqrt{Eh^3}(L^2+2a_2L-a_2^2)} \tag{2.39}$$

If the interlaminar shear forces in the overhanging sections are ignored, the displacement δ becomes:

$$\delta = \frac{\sqrt{G_C}(-9L^4-16a_2L^3+20a_1L^3+18a_2^2L^2+36a_1a_2L^2-36a_1a_2^2L+12a_1a_2^3+3a_2^4)}{12\sqrt{Eh^3}(L^2+2a_2L-a_2^2)} \tag{2.40}$$

Note that Eqn. (2.40) is still applicable to the case that the interlaminar shear forces in the overhanging sections are ignored.

The prediction of the above analytical expressions for the load-displacement curve is schematically demonstrated in Figure. 2.7, showing the change with respect to the increase of a_1 and G_C.

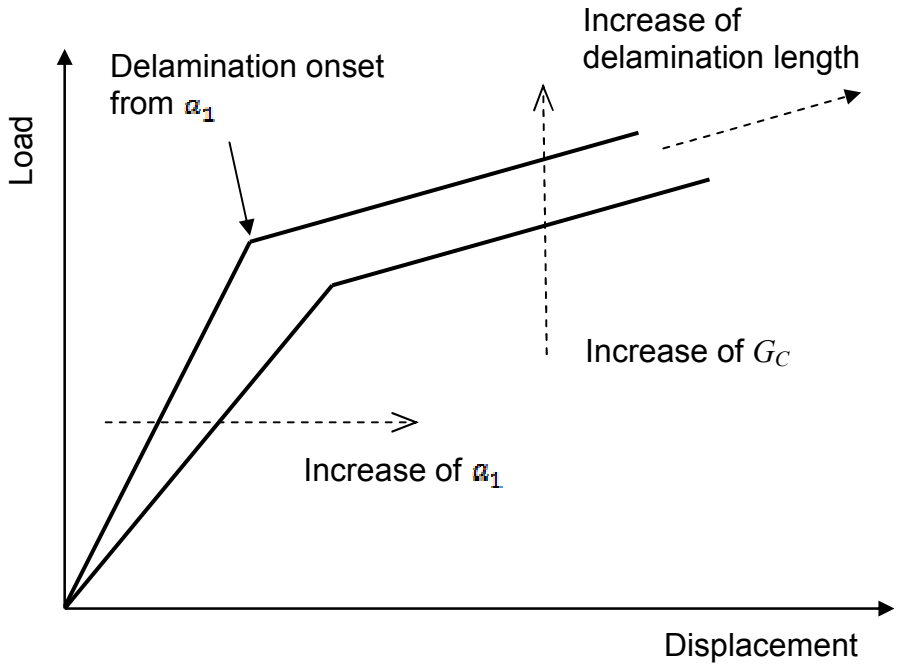

Figure 2.7 Schematic diagram of load-displacement curve of the INF test

Note that for the curves in Figure. 2.7, the initial slope of the load-displacement curve is determined using Eqn. (2.32) and the second slope, during the delamination growth, using Eqn. (2.38) and (2.39).

2.4 Prediction of Delamination Growth Rate and Discussion

Note that since the differentiation of Eqn. (2.37) with respect to a_1 always yields a negative value, the INF test generates stable delamination growth as long as the growth is along direction a_1 only. Furthermore, time derivative of Eqn. (2.40) suggests that delamination growth rate $\dot{a_1}$ is a linear function of $\dot{\delta}$:

$$\dot{a_1} = \frac{12\left(L^2+2a_2L-a_2^2\right)\sqrt{Eh^3}}{\sqrt{G_C}\left(20L^3+36a_2L^2-36a_2^2L+12a_2^3+\frac{9}{2}(L-a_2)^3\right)}\dot{\delta} \tag{2.41}$$

That is, with a_2 and G_C being constant, the INF test can be conducted at different crosshead speeds, without concerns about the stability of delamination growth. This is an advantage of INF test, especially for the study of the influence of crack growth rate on the delamination development. Therefore, the test can be used to study influence of loading rate on the delamination resistance.

As evident in Figure 2.8, the predictions of delamination growth using the analytical solutions in ref. [16] and the current revised solutions are demonstrated using the load-displacement curve with respect to a constant physical crack length a_1 and G_C. It should also be noted that these curves are constructed based on the assumption of stress-free fracture surfaces that do not impose any barrier for the delamination growth. Schuecker and Davidson [19] utilized the 4ENF test specimen to analyze the effect of friction on G for pure mode II using finite element analysis and found that it only increases the G_{IIC}value by no more than 2%. Therefore, in this study, the effect of friction on G_C is neglected for simplicity and with this assumption, according to Eqn. (2.38) and (2.39), the slope of the P-δ curve during the delamination growth should be independent of the $G_C$value.

It should be pointed out that the analytical expression in ref. [16] and current version have the same expressions for energy release rate G_{a_1}but different for G_{a_2}.The critical energy release rate G_c = 3190 J/m^2 in Figure 2.8, is computed using eq. (2.37) with the specimen data in Table 2.1.

Comparison of the difference in percentage for the compliance and displacement for specimen dimensions given in Table 2.1 are 11.7% and 7.2% respectively. This

difference is due to neglecting shear deformation in the overhanging sections of the INF specimen in the analytical solution given in ref. [16].

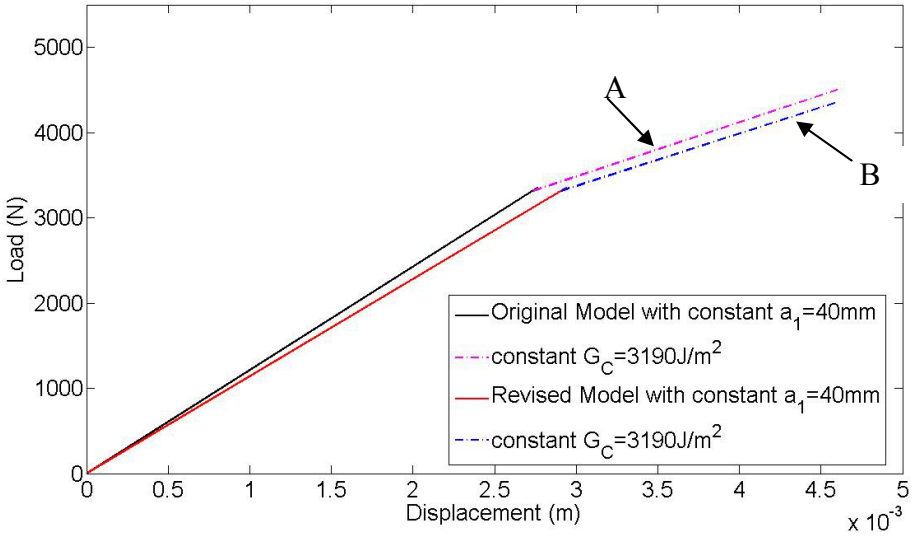

Figure 2.8 Comparison of load-displacement curve generated by analytical solutions in ref. [16] and current revised solution with G_c = 3190 J/m^2. The curve labeled as "A" is generated from ref. [16] based on physical crack length, and that labeled as "B" is generated from current revised solution based on physical crack length

Table 2.1 Material property and dimensions of the analytical model of INF specimen (Refer to Figure 1 for the notation)

E (GPa)	v	a_1 (mm)	a_2 (mm)	h (mm)	L (mm)	w (mm)	KA (mm)	DE (mm)
26.5	0.3	40	12	3.1	30	20	50	40

*The material constant values were adopted from ref. (14).

2.5 Concluding remarks

In this chapter, a revised analytical model of the INF specimen to characterize mode II fracture toughness of fiber composites is developed. The model is base on Timoshenko beam theory and considers the effect of interlaminar shear in the overhanging section on the compliance and global deformation of the specimen. Explicit expressions for compliance and displacement derived here indicated that the interlaminar shear stress variation has a significant contribution and hence must be incorporated in the analytical solution. The drawback of the analytical approach is that its application is generally restricted to problems that involve simple geometry, loads or boundary conditions with linear elastic systems.

Chapter 3 Finite Element Simulation of Stable Delamination Development

3.1 Introduction

The study of delamination process commonly involves two stages: initiation and growth. Delamination initiation is related to the inter-laminar strength of the material and in many applications stress-based criteria have been used to predict it. Delamination growth has been widely investigated using the theory of fracture mechanics through analytical and numerical approaches. The finite element method can be used to calculate fracture parameters such as energy release rate (G), stress intensity factor (K) or J-integral (J) that serves as a driving force for crack growth. Techniques such as the compliance derivative technique (CDT), virtual crack closure technique(VCCT) or J-integral can be used to calculate energy release rate (G), and predict delamination growth by comparing G values to the critical value (G_C) which is the material's resistance to fracture. However, all these techniques can't be directly applied to predict delamination without an initial crack and further complication of the finite element implementation of those methods arises when progressive delamination is involved.

An alternative solution to avoid the above difficulties is to model delamination development using cohesive zone model. As shown in Figure 3.1, in this approach, a cohesive damage zone is developed near the crack front. Material behavior in the cohesive zone follows a cohesive constitutive law which adopts a softening relationship between

cohesive traction (σ) and relative displacement (δ) between the upper and lower substrate layers, with the area under the curve being the critical fracture energy (G_C). When an external load is applied to the pre-cracked body, the adjacent substrate layers which are held by cohesive traction (tensile and/or shear), separate gradually. A complete failure that leads to crack growth would occur behind the crack front when the separation of these layers reaches a critical value at which the cohesive traction vanishes across the substrate layers.

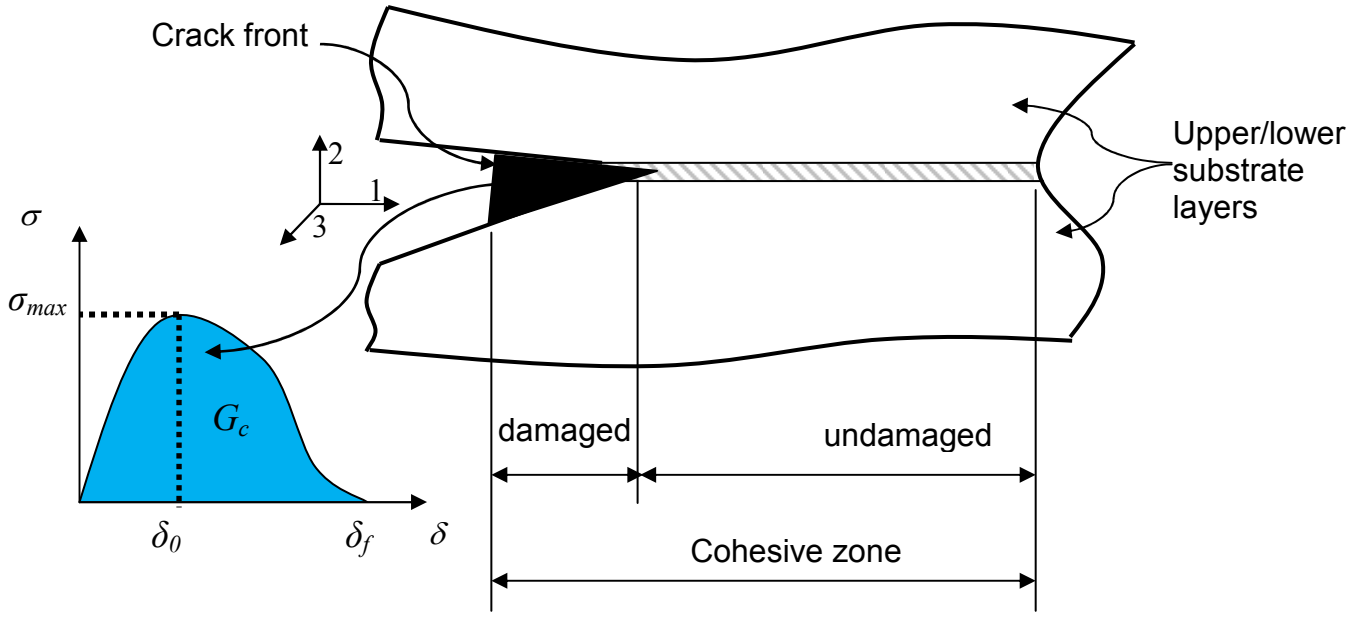

Figure 3.1 Schematic diagram of the cohesive zone model.

The cohesive zone model was implemented in finite element framework using a special set of interface elements [10, 20-22]. Introducing interface elements in FE analysis of delamination requires a finite stiffness prior to onset of delamination as well as delamination initiation and growth criteria. Therefore, the interface elements, equipped with the cohesive constitutive relation, has been utilized for simulating delamination process in FRP and numerous FEM works using interface elements have been published

in the literature [23-25] . However, like the other numerical techniques mentioned earlier, application of this method is limited to prediction of delamination with an initial crack. Disadvantage of the interface elements and other methods such as the use of spring elements to implement the cohesive zone model in FEM are well documented [26].

To overcome the limitation of interface elements, Fan et al. [27] introduced a new approach to implement the cohesive zone model in FEM using solid elements with cohesive damage material property. Unlike the interface elements where the delamination initiation criterion is described by a combination of only tensile and shear traction components, solid elements have all stress components so that multi-axial-stress-based damage initiation criteria can be adopted. Furthermore, the constitutive law of the cohesive damage material model assumes a linear-elastic response prior to the onset of delamination and the linear softening law for damage evolution, based on the concept of linear fracture mechanics.

However, in many practical applications, there could be a substantial plastic deformation in the resin rich region where delamination growth should not be based on linear elastic damage material model. In this regard, there are many damage material models in the literature to simulate the delamination development using cohesive elements. For example, in ref. [33] elastic-plastic cohesive zone model is used to study facture behavior of metal-matrix composites under elastoplastic deformation. In ref. [34] inter-laminar delamination process was modeled using 3D elastic-plastic finite element model in ABAQUS. However, these damage models were implemented using cohesive elements with a traction-separation constitutive relation, which has some intrinsic limitations. Therefore this study investigates delamination growth undergoing plastic

deformation in the inter-laminar region using solid elements with damage material property. The formulation of plastic deformation of the material in the inter-laminar region is based on von Mises criteria. The simulation of delamination growth involves gradual degradation of material stiffness along the inter-laminar region ahead of the crack tip. The constitutive equation of the material in the inter-laminar region is described by elastic-plastic damage material model. Compared to the cohesive elements, this damage material model has the advantage of being able to adopt a multi-axial-stresses-based delamination initiation criterion. Besides, the proposed elasto-plasitc damage material model uses strain energy to define the damage status.

This chapter is organized as follows. Section 3.2 provides the FE analysis of delamination growth using cohesive elements, tailored for application to INF test. The FE solution will be used to verify the revised analytical expressions for compliance of the INF specimen and its energy release rate for delamination derived in chapter 2. Based on the FE model, damage evolvement in front of the crack tip is investigated, and the use of an effective crack length to replace physical crack length for calculation of G is discussed. Section 3.3 summarizes the new proposed elastic-plastic damage material model. Section 3.4 describes the finite element simulation of delamination growth using solid elements with the elastic-plastic damage material model properties tailored for an application to double-edge-notched tensile (DENT) specimen, double-cantilever-beam (DCB) specimen and internal-notched-flexure (INF) test and. Finally, section 3.5, presents some concluding remarks.

3.2 Cohesive Elements

3.2.1 Finite Element Model of INF Specimen using Cohesive Elements

Delamination growth in the INF model shown in Figure 2.2 is studied using cohesive elements to validate the analytical expressions for compliance and energy release rate derived in chapter 2. A two- dimensional FE model of INF specimen was created using a commercial code ABAQUS/Standard v6.9 [28]. Overall length of the model is 160 mm, of which dimensions for each section are listed in Table 2.1. The model has three layers. The top and bottom layers represent substrates of the composite material, consisting of 4-node, plane-strain elements (CPE4I) with incompatible mode of orthotropic elastic properties. The middle layer represents the interlaminar region which includes initial crack lengths of 40 mm for a_1 and 12 mm for a_2. A frictionless, small sliding contact is defined between the crack surfaces to avoid penetration. The un-cracked region in the middle layer consists of cohesive elements (COH2D4) that are connected with the top and bottom layers using mesh-tie constraint. Dimensions of the cohesive elements are 0.02 × 0.02 mm; while those in the top layers are 0.25 × 0.25 mm and in the bottom layer 0.5 × 0.5 mm. Totally, 4596 elements were used to model the top and bottom layers, and 2160 elements for the middle layer. Figure 3.2(a) shows the overall mesh pattern of the model, and Figure 3.2(b) the detailed mesh pattern around the interlaminar region. An example of the deflection behavior during the delamination growth is given in Figure 3.2(c).

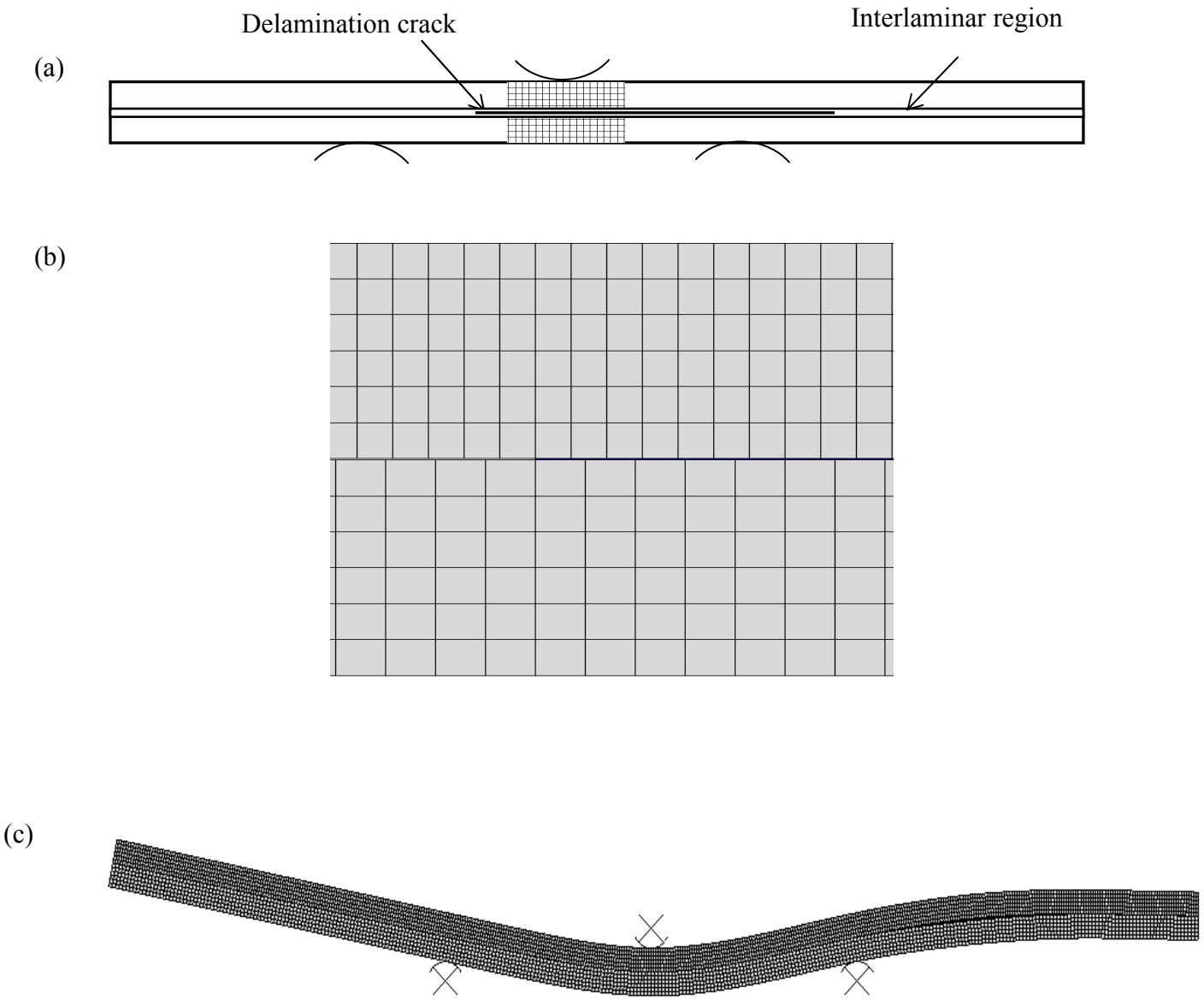

Figure 3.2 Finite-element model of the INF specimen: (a) the overall mesh pattern, (b) mesh pattern around the inter-laminar region, and (c) an example of the deflection behavior.

Values used in ref. (14) were adopted as input material properties for the top and bottom layers and are given in Table 3.1. Material constants for the middle layer are given in Table 3.2 and these constants are used to define constitutive equation of the cohesive elements based on a bilinear traction-separation law for fracture. Interface stiffness values in Table 3.2 are defined as $K_{nn} = \frac{E_m}{t}$ and $K_{ns} = K_{ss} = \frac{\mu_m}{t}$ where t is thickness of the interlaminar region, E_m and μ_m are the elastic moduli of the interlaminar matrix for tension and shear, respectively, v_m Poisson's ratio, and $\mu_m = \frac{E_m}{2(1+v_m)}$. The quadratic traction-interaction failure criterion [28] is selected for damage initiation, and critical energy release rate (G_C) for crack propagation in a mixed mode of tension (mode I) and shear (mode II) is defined in terms of G_{IC} and G_{IIC} based on the B-K criterion [31]. In this study, the model is subjected to displacement up to 4.5 mm at the loading pin.

Table 3.1. Dimensions of the FE model of INF specimen (Refer to Figure 2.2 for the notation)

a_1 (mm)	a_2 (mm)	h (mm)	L (mm)	w (mm)	KA (mm)	DE (mm)
40	12	3.1	30	20	50	40

Table 3.2. Mechanical properties for top and bottom layers of the INF FE model

E_{11} (GPa)	$E_{22} = E_{33}$ (GPa)	$\mu_{12} = \mu_{13}$ (GPa)	$v_{23=} v_{12} = v_{13}$
26.5	6.0	6.0	0.3

Table 3.3. Properties of cohesive elements at the interlaminar interface of the FE model

E (MPa)	K_{nn} (MPa)	K_{ns} (MPa)	K_{ss} (MPa)	G_{IC} (J/m^2)	G_{IIC} (J/m^2)	η	Y (MPa)	S (MPa)	v
3000	150000	57692	57692	500	2500	0.0*	72	40	0.3

*for pure shear mode

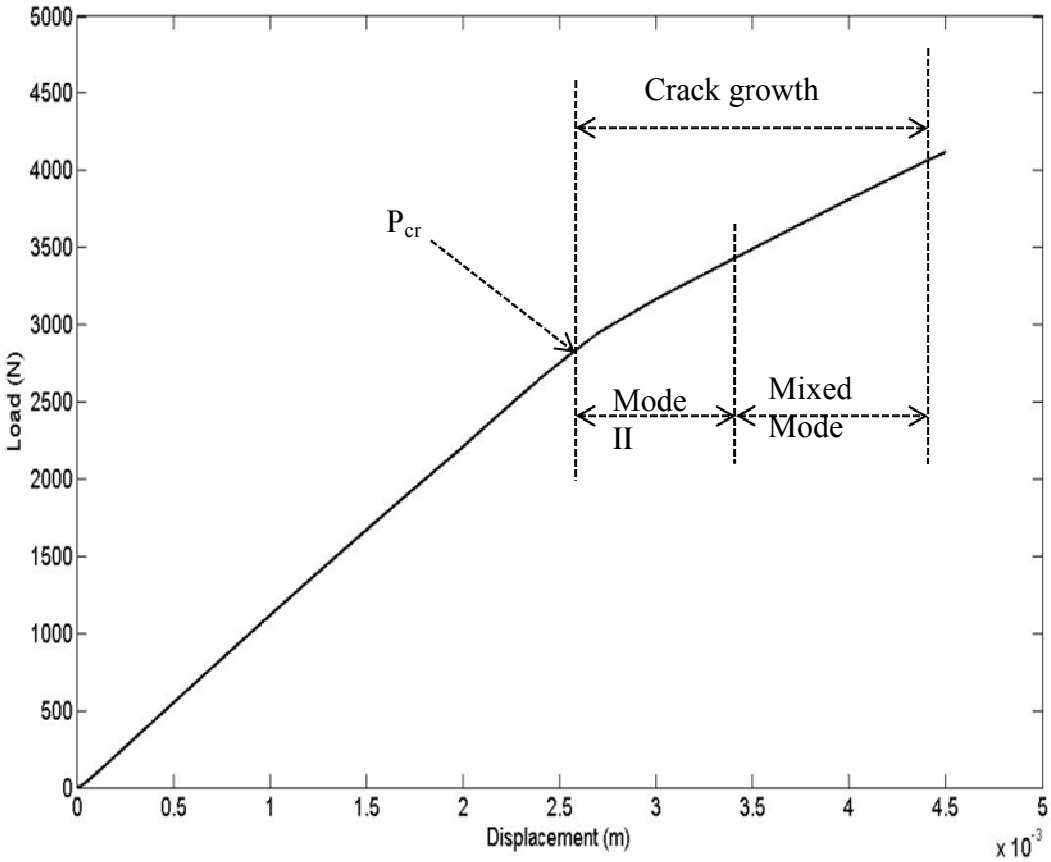

Figure 3.3 Load-displacement curve of the INF specimen from FE model.

Figure 3.3 shows a load-displacement response of the INF specimen generated by the FEM solution, where the point indicates the initiation of delamination growth.

When a cohesive element in front of the crack tip is completely damaged, it is assumed that delamination starts to grow and this is taken as a reference to the crack tip position. In view of this assumption, the FE result shows that delamination commences when the applied load reaches a critical value of $P_{cr} = 2988N$. After initiation, the delamination grows along the interface and the load, P increases linearly with displacement, ensuring the stability of the delamination growth and it is found that the crack length a_1 has grown from 40 to 61mm (equivalent to the total crack length of (a_1+a_2) increasing from 52 to 73 mm). However, after initiation, the delamination crack grows a short distance (about 7mm) in pure mode II and then the crack continued to grow in a mixed mode behavior as shown in Figure 3.3. The finite element result together with a similar experimental observation (being conducted by another researcher, K. Brethome, at the time of writing this thesis) leads to the conclusion that the INF specimen generates pure mode II delamination for small deformation, i.e. in the beginning of delamination growth. For large deformation, it generates a mixed mode delamination growth and this problem needs further investigation.

Figure 3.4 shows the load-displacement response with respect to the variation of a_1 based on the condition in Eqn. (2.36) and the result ensures that the delamination growth is always in the a_1 direction only.

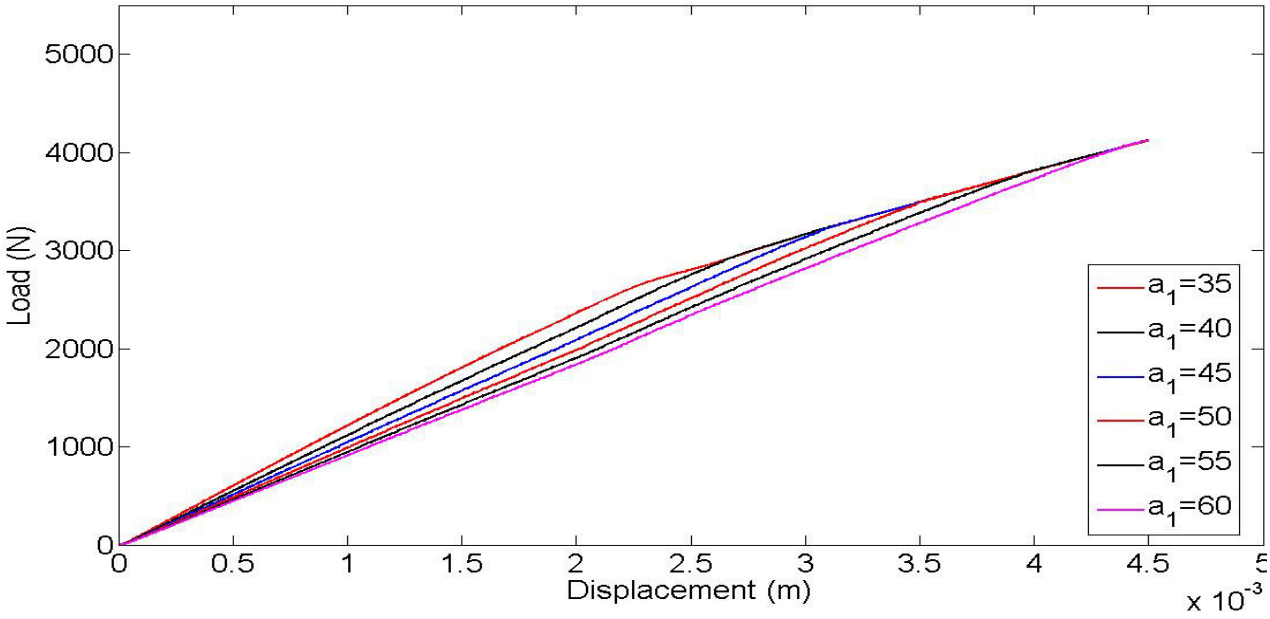

Figure 3.4 Load-displacement curve of the INF specimen from different crack lengths.

Figure 3.5 compares load-displacement curves generated by the FE model and that from Eqns. (2.1) and (2.32) based on values given in Tables 3.1-3.2. Note that flexure modulus E and shear modulus μ in Eqns. (2.1) and (2.32) are equal to E_{11} and μ_{12}, respectively, in Table 3.2 and $\kappa = 0.867$ for a rectangular cross section [17]. The figure suggests that before delamination growth, the initial slope of the load-displacement curve from the FE model coincides with that predicted from Eqn. (32) but lower, though only slightly, than that from Eqn. (2.1). Based on values given in Tables 3.1 and 3.2, contribution to value for C from four terms on the right-hand side of Eqn. (2.32) is 47.5%, 2.6%, 44.2% and 5.7%, respectively, indicating that difference of the compliance caused by the consideration of interlaminar shear force in the overhanging section is only about 6%. The corresponding G_{a_1} values show no difference between Eqns. (2.2) and (2.34a).

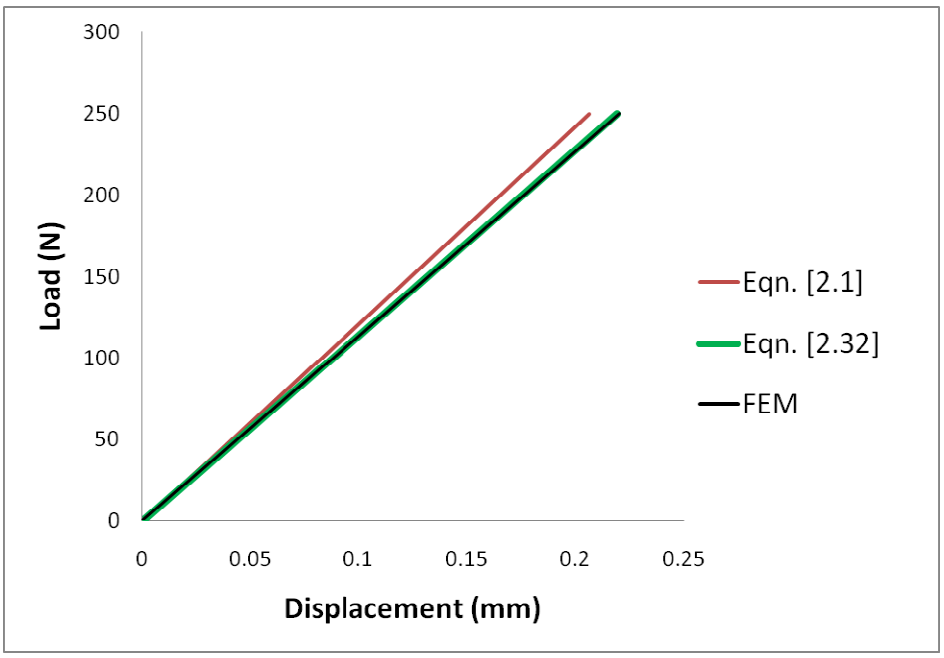

Figure 3.5 Comparison of load-displacement curves before delamination initiation, generated by the FE model, Eqn. (1) and Eqn. (32).

Delamination damage process Zone

Results from the FE model suggest that an extensive damage exists at the crack tip before delamination growth commences. Therefore, the use of a physical crack length in the analytical expressions for G, as calculated using Eqn. (2.37) in chapter 2, severely overestimate the interlaminar fracture toughness ($G_c = 2500$ J/m^2) used in the FE model. Hence, an effective crack length (a_e) should be used. This effective crack length is a correction made to the physical crack length (a_1) by taking into account the size of the damage extent in the material ahead of the crack tip. The damage process zone is defined as the part of the interface layer ahead of the crack tip where cohesive layer softens and the length of the process zone (a_p) at the moment of delamination growth is evaluated by studying the extent of damaged elements in front of the crack tip along the interface layer using finite element simulation. The state of damage in a cohesive element is described

by a scalar damage variable D in the constitutive equation of the cohesive element where its value range is from 0 (without damage) to 1, (completely damage). When the cohesive element is completely damaged , this will be taken as a reference to the crack tip position. All cohesive elements from the crack tip which are partially damaged , are added to the list of process zone. Hence, the total length of the damage process zone is determined by multiplying the total number of partially damaged cohesive elements with the element size along the interface layer. This process is demonstrated in Figure 3.6 and the FE analysis result shows that when the delamination started to grow , the process zone reaches about 8 mm which means that all the elements in this length are partially damaged. This result gives useful information from which the size of the damage zone (a_c) that will need to be considered to correct the physical crack length.

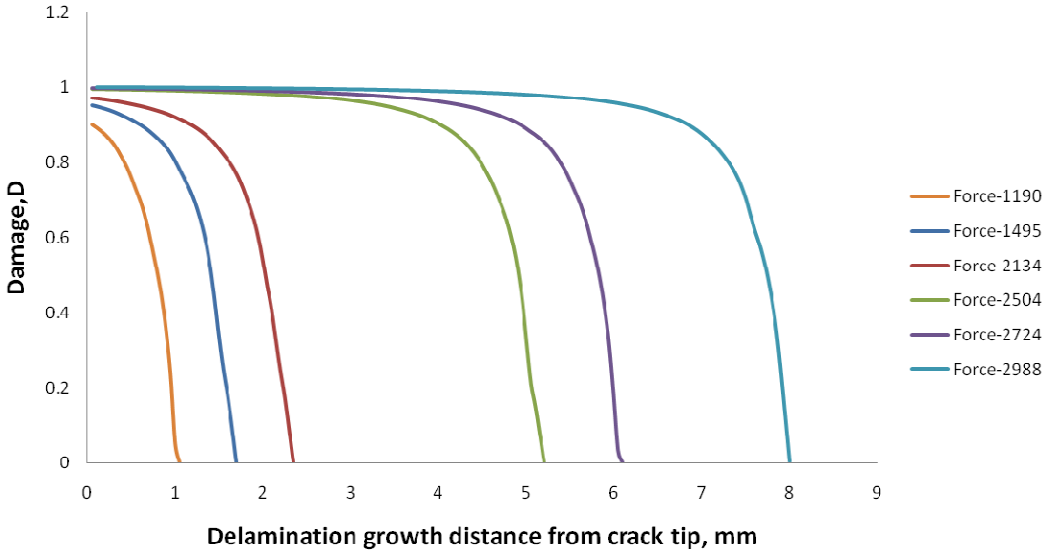

Figure 3.6 Plot of the damage zone length as a function of delamination growth distance from the right crack tip.

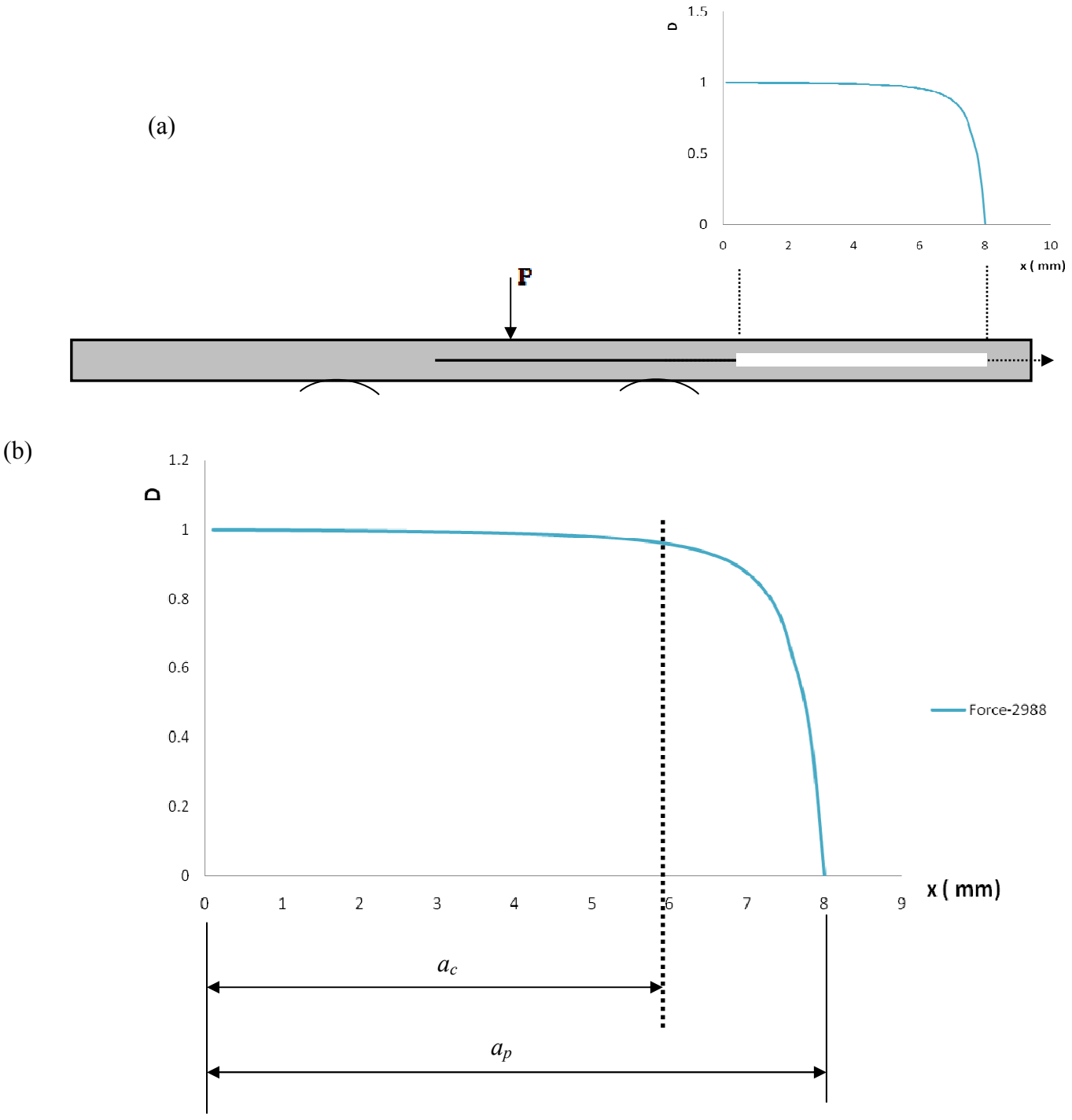

Figure 3.7 Depiction of damage development in front of the right crack tip at the critical load for delamination initiation. Note that D = 1 for full damage development and D = 0 for no damage.

The effective crack length is defined as:

$$a_e = a_1 + a_c \tag{3.1}$$

where a_e is the effective crack length, a_1 is the physical crack length, and a_c the crack length contributed from the damage zone of which the value is determined by a fitting process.

After delamination is initiated, the analytical load-displacement response of the INF specimen is predicted based on the effective crack length, i.e., the physical crack length (a_1) in the analytical expressions for G, load (P) and displacement (δ), as given in section 2.3 of chapter 2, is replaced with the effective crack length (a_e). Now, an estimate of the new crack length (a_c) can be obtained by comparing the analytical load-displacement curve with the FE solution through a fitting process. Thus, it is observed that with a_c = 5.875 mm, expression for G based on the effective crack length yields a value very close to the input G_c value for the cohesive elements, as shown in Figure 3.8.

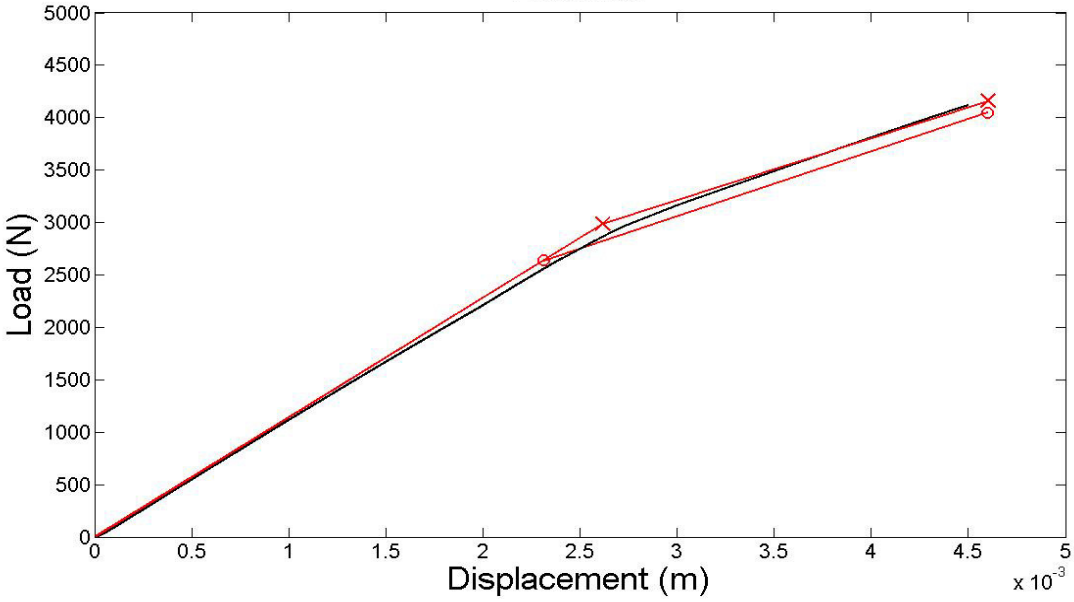

Figure 3.8 Comparison of load-displacement curve generated by the FE model and those by Eqn. [32] with G_c = 2500 J/m^2. The curve marked as "○" is generated from Eqn. [32] based on physical crack length, and that marked as "×" is generated from the same equation based on effective crack length.

3.3 Elastic-plastic damage material

When substantial plastic deformation is involved in the resin rich region of FRP, modeling the inter-laminar region based on linear elastic damage material model will be obviously invalid. Therefore, this part of the study is to investigate delamination growth after undergoing plastic deformation in the interlaminar region. The plasticity formulation in the inter-laminar region is based on von Mises criteria with isotropic hardening. The simulation of delamination growth involves gradual degradation of stiffness of material

along the interface region ahead of the crack tip. The proposed material model will be implemented into the commercial FE software ABAQUS via a user-defined material subroutine (UMAT). The UMAT will govern the behavior of the material during the different loading states, i.e., elastic, inelastic, damage initiation and propagation. In this chapter, all stresses are expressed according to the local coordinates shown in Figure 3.1.

3.3.1 Constitutive relationship

The constitutive response of the material in the inter-laminar region is described by continuum solid elements with elastic-plastic damage material model. An isotropic damage model is assumed.

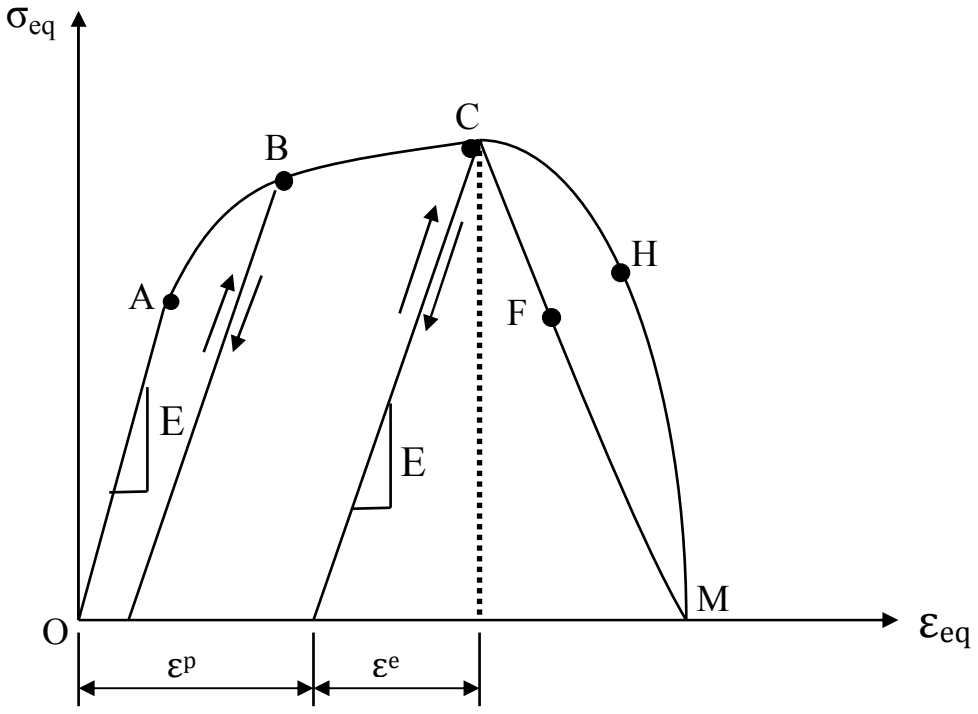

Figure 3.9 Schematic diagram of elastic-plastic damage material model response.

In Figure 3.9, a schematic diagram of elastic-plastic damage material model is shown. The response of the undamaged material which is shown by the initial part of the curve (OA) is assumed to be linearly elastic. Point *A* is a yield point where the onset of permanent strain is initiated. In multi-axial stress state, this yield point is often denoted a yield/loading surface. The part of the curve (AC) denotes an elasto-plastic response which is also said to introduce a "hardening" mechanism, with a damage initiation point at the maximum equivalent stress, point C. This point is denoted by delamination onset surface in multi-axial stress state. The plastic stiffness during hardening will be calculated using the hardening law. The portion of CH or CF reflects a "softening" mechanism and the stiffness of softening will be determined using the damage evolution criteria. Unloading is assumed to take place as a purely elastic process with the initial stiffness. Reloading after unloading gives elastic response up to a new yield point B.

The key factors required to describe the basic principle in the elastic-plastic damage material model are summarized as follows:

1. A decomposition of total strain into elastic and plastic contributions:

$$d\varepsilon_{ij} = d\varepsilon_{ij}^{e} + d\varepsilon_{ij}^{p} \tag{3.2}$$

where $d\varepsilon_{ij}$ is increment of total strain, $d\varepsilon_{ij}^{e}$ is increment of elastic strain, and $d\varepsilon_{ij}^{p}$ is increment of plastic strain

A governing principle for the elastic contribution:

$$d\varepsilon_{ij}^{e} = E_{ijkl}^{-1} d\sigma_{kl} \tag{3.3}$$

where E_{ijkl} is the initial elastic stiffness

2. Factors that control plastic deformation are:

(a). Yield criterion

(b). Plastic flow rule

(c). Hardening law

3. Damage initiation criterion

4. Damage evolution criterion

Elastic Behavior

The basic principle of the elastic-plastic damage material model is applied to a plain-strain condition formulation and the elastic part is related to Cauchy stress through linear elastic constitutive model as:

$$d\sigma_{ij} = E_{ijkl} d\varepsilon^{e}_{kl} \qquad (i, j, k, l = 1, 2, 3) \tag{3.4}$$

where E_{ijkl} is Young's modulus and for plane strain condition is given as:

(3.5)

Yield Criterion

The onset of plastic deformation is predicted by adopting a von Misses yield criteria which is defined in terms of equivalent stress (σ_{eq}) and isotropic hardening equivalent stress ($Y\left(\bar{\varepsilon}^{p}\right)$).

$$f\left(\sigma_{eq}, Y\left(\bar{\varepsilon}^{p}\right)\right) = \sigma_{eq} - Y\left(\bar{\varepsilon}^{p}\right) \geq 0 \tag{3.6}$$

Where σ_{eq} and $Y\left(\bar{\varepsilon}^{p}\right)$ are defined as:

$$\sigma_{eq} = \frac{1}{\sqrt{2}}\sqrt{\left(\sigma_{11}-\sigma_{22}\right)^2 + \left(\sigma_{11}-\sigma_{33}\right)^2 + \left(\sigma_{22}-\sigma_{33}\right)^2 + \psi\left(\tau_{12}^2 + \tau_{13}^2 + \tau_{23}^2\right)} \tag{3.7}$$

$$Y\left(\bar{\varepsilon}^{p}\right) = \sigma_{y} + R\bar{\varepsilon}^{p} \tag{3.8}$$

Where σ_y is yield stress, $\bar{\varepsilon}^p$ is an accumulated plastic strain and R represents the slope of the isotropic strain hardening (see Figure 3.10). The corresponding equivalent total strain is:

$$\varepsilon_{eq} = \frac{\sqrt{2}}{3}\sqrt{(\varepsilon_{11}-\varepsilon_{22})^2 + (\varepsilon_{11}-\varepsilon_{33})^2 + (\varepsilon_{22}-\varepsilon_{33})^2 + \psi(\varepsilon_{12}^2 + \varepsilon_{13}^2 + \varepsilon_{23}^2)} \tag{3.9}$$

The parameter ψ in Eqns. (3.7) and (3.9) is defined in terms of the tensile (T) and shear strength (S) of the material in the inter-laminar region. The expression for ψ is derived based on the assumption that $(\sigma_{22} = \sigma_{33})$ in Eqn. (3.7) for uniaxial tensile test under ideal case and making use of the tensile (T) and shear strength (S) of the material as an allowable stress limit for yielding. For von Mises criterion, $\psi = 6$.

$$\psi = 2\left(\frac{T}{S}\right)^2 \tag{3.10}$$

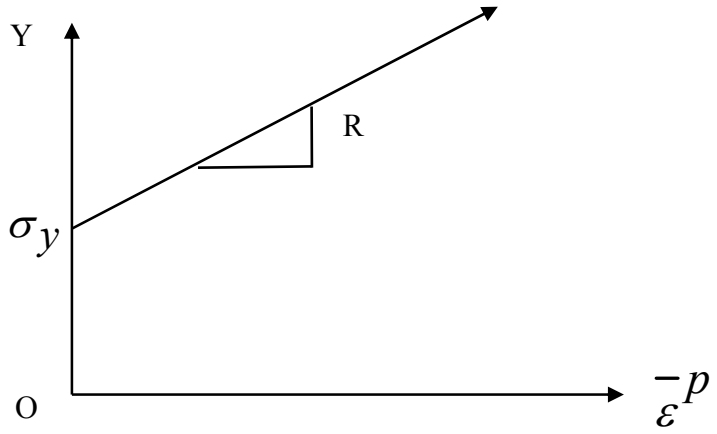

Figure 3.10 Schematic diagram of linear isotropic strain-hardening curve

Flow rule

Plastic strains is developed by loading beyond the yield i.e. whenever $f\left(\sigma_{eq}, Y\left(\bar{\varepsilon}^{p}\right)\right)=0$, which is always assured by the consistency condition during loading (i.e. stress must be on yield surface at all times). Thus, magnitude of the increment of plastic strain can be evaluated from the hardening behavior of the material and must be related to stress increment through the definition of associated plastic flow rule, derived from yield surface, as:

$$d\varepsilon_{ij}^{p}=\lambda\frac{\partial f}{\partial\sigma_{ij}} \tag{3.11}$$

where $\lambda=d\bar{\varepsilon}^{p}$, a positive scalar plastic multiplier, determined from the consistency condition. This shows that for small stress increment

$$df=0 \tag{3.12a}$$

$$\frac{\partial f}{\partial\sigma_{ij}}d\sigma_{ij}+\frac{\partial f}{\partial d\bar{\varepsilon}^{p}}d\bar{\varepsilon}^{p}=\frac{\partial f}{\partial\sigma_{ij}}d\sigma_{ij}+\frac{\partial f}{\partial Y}\frac{\partial Y}{\partial d\bar{\varepsilon}^{p}}d\bar{\varepsilon}^{p}=0 \tag{3.12b}$$

Using Eqns. (3.6) and (3.8), we obtain, $\frac{\partial f}{\partial Y}=-1$, $\frac{\partial Y}{\partial d\bar{\varepsilon}^{p}}=R$ and substituting in Eqn. (3.12b), we get.

$$\frac{\partial f}{\partial\sigma_{ij}}d\sigma_{ij}=R\lambda, \qquad \lambda=d\bar{\varepsilon}^{p} \tag{3.12c}$$

Making use of Eqns. (3.2), (3.4), the stress increment, $d\sigma_{ij}$, in Eqn. (3.12c) can be expressed as:

$$d\sigma_{ij}=E_{ijkl}\left(d\varepsilon_{ij}-d\varepsilon_{ij}^{p}\right)=E_{ijkl}\left(d\varepsilon_{ij}-\lambda\frac{\partial f}{\partial\sigma_{ij}}\right) \tag{3.13}$$

Thus, from Eqns. (3.12c) and (3.13), the plastic multiplier λ is obtained as:

$$\lambda = \frac{\frac{\partial f}{\partial \sigma_{ij}} E_{ijkl} d\varepsilon_{kl}}{R + \frac{\partial f}{\partial \sigma_{ij}} E_{ijkl} \frac{\partial f}{\partial \sigma_{kl}}} \tag{3.14}$$

Under plastic straining, the flow rules are incremental and hence stress increments are related to strain increments using incremental constitutive relation. While the stress increment in elastic deformation is given by Eqn. (3.13), the stress increment in plastic deformation is given by

$$d\sigma_{ij} = E^{ep}_{ijkl} d\varepsilon_{ij} \tag{3.15}$$

where E^{ep}_{ijkl} is elasto-plastic tangent modulus.

By substituting Eqn. (3.14) into Eqn. (3.13) and equating with Eqn. (3.15), the elasto-plastic tangent modulus, E^{ep}_{ijkl}, is:

$$E^{ep}_{ijkl} = E_{ijkl} - \frac{E_{ijab} \frac{\partial f}{\partial \sigma_{ab}} \frac{\partial f}{\partial \sigma_{cd}} E_{cdkl}}{R + \frac{\partial f}{\partial \sigma_{mn}} E_{mnrs} \frac{\partial f}{\partial \sigma_{rs}}} \tag{3.16}$$

The elastic-plastic damage material adopts the isotropic damage elastic constitutive relationship once the damage initiation criterion is satisfied. Denoting on *d* as a scalar damage variable at a local material point, the physical stress could be related to the strain by

$$\sigma_{ij} = \overline{E}_{ijkl} \varepsilon_{kl} \qquad (i, j = 1, 2, 3) \tag{3.17}$$

where $\overline{E}_{ijkl}$ is the elastic stiffness in the damaged state which is a function of the damage variable, *d*. For linear material softening shown by curve BN in Figure 3.11, the stiffness

in the damaged state can be determined from the geometry of the same figure and is given by

$$\overline{E}_{ijkl} = E_{ijkl}\left(1 - \frac{2U_c d}{U_0(1-d) + 2U_c d}\right) \tag{3.18}$$

where U_C is critical strain energy at a complete failure of the loaded element and is considered as a material property. U_0 is the strain energy when damage initiation occurs in the material for the first time and can be calculated as:

$$U_0 = (\int \sigma_{ij} d\varepsilon_{ij})\,|_{e\geq 1} \qquad (i, j = 1, 2, 3) \tag{3.19}$$

where e is a non-dimensional parameter that is used to show the condition for damage initiation in a material. The value ($e \geq 1$) indicates a critical condition for damage initiation is reached and the details will be discussed later in section 3.3.2.

The range of d value is from 0 (without damage) to 1 (completely damaged). When the damage is fully developed, i.e. d = 1, the stiffness given by Eqn. (3.18) drops to zero and the material cannot withstand any types of load. Since this result possibly leads to the penetration between the neighboring substrates in FRP, stiffness degradation in the out-of-plane direction (2-direction in Figure 3.1) is prohibited when the compressive strain occurs in that direction.

$U_0 = A_{DBF}$
$U_D = A_{DBC}$
$U_C = A_{DBN}$

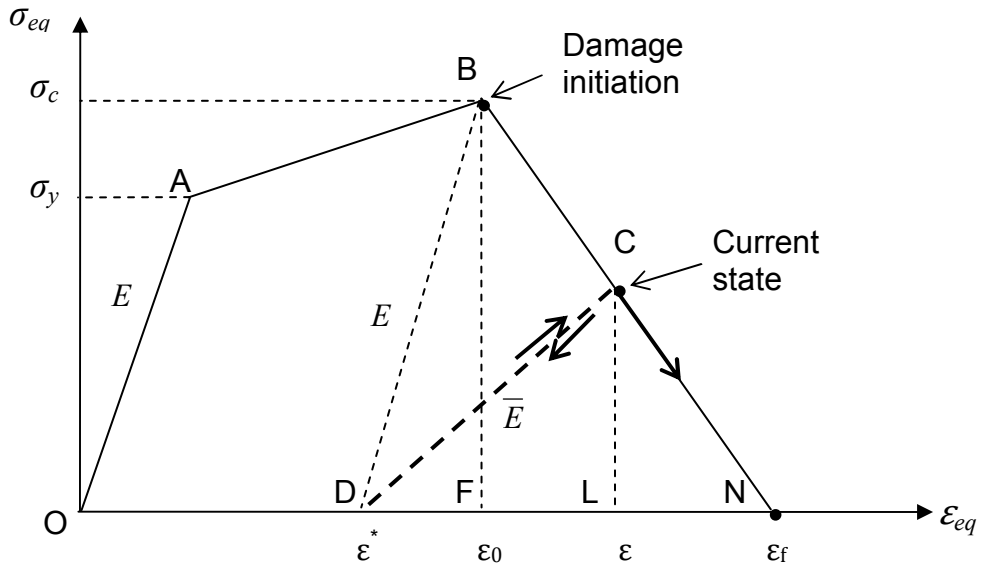

Figure 3.11 Schematic diagram of elastic-plastic damage material model with linear softening

In Figure 3.11, U_D is the energy absorbed by any deformation mode at the current loading state after delamination is initiated and can be determined by integrating the energy dissipated in a given fracture mode. For example, for a linear material softening condition, at the current loading state shown in Figure 3.11, U_D is given by the area (A_{DBC}) as:

$$U_D = \frac{\sigma_C U_C (\varepsilon - \varepsilon_0)}{2(U_C - U_0)} \tag{3.20}$$

where σ_C and ε_0 are the maximum equivalent stress and corresponding equivalent strain, respectively, when a damage initiation criterion is satisfied at the first time, and ε is the equivalent strain at the current stress state.

The value range for U_D is from 0 (when $\varepsilon = \varepsilon_0$) to U_C, i.e., when the damage is fully developed (d = 1 at which $\varepsilon = \varepsilon_f$). When d = 1, the dissipated energy reaches its critical value, U_C.

3.3.2 Damage initiation criterion

Depending on the normal stress component (σ_{22}) being positive or negative, the following damage initiation criterion is proposed.

$$e^2 = \begin{cases} \left(\frac{\sigma_{11}^2 + \sigma_{22}^2 - (\sigma_{11}\sigma_{22} + \sigma_{11}\sigma_{33} + \sigma_{22}\sigma_{33}) + \sigma_{33}^2}{T^2}\right) + (\tau_{12}^2 + \tau_{13}^2)/S^2 & (\text{for } \sigma_{22} > 0) \\ (\tau_{12}^2 + \tau_{13}^2)/S^2 - \alpha^2\left(\frac{\sigma_{11}^2 + \sigma_{22}^2 - (\sigma_{11}\sigma_{22} + \sigma_{11}\sigma_{33} + \sigma_{22}\sigma_{33}) + \sigma_{33}^2}{T^2}\right) & (\text{for } \sigma_{22} \le 0) \end{cases}$$

(3.21)

where τ_{12} and τ_{13} are shear stresses, α a non-dimensional parameter that is used to quantify the effect of the compressive stress on the suppression of delamination and is determined using the critical load for damage initiation, *T and S* are transverse tensile and shear strength of the material in the interface, respectively. The value of *e* determines whether the critical condition for damage initiation is reached. That is, the damage is initiated when *e* is equal to or larger than 1.

The damage initiation criterion reflects the phenomenon that compressive stress may slow down or suppress the damage initiation [29].

3.3.3 Damage evolution law

As shown in Eqn. (3.18), the material softening is fully governed by the evolution of a damage variable *d*. The damage parameter *d* can be defined by any monotonically increasing function, valued from 0 to 1, of any state variables such as stresses, strains or strain energy. In this study, the evolution of *d* is expressed in terms of the critical strain energy (U_C) and the present state of energy absorbed by the deformation (U_D).

$$d = \frac{U_D^m}{U_C - U_D + U_C^m} \tag{3.22a}$$

where *m* is a non-dimensional parameter selected to allow change of damage evolution law. For a linear system, *m*= *1*, the value of *d* is:

$$d = \frac{U_D}{2U_C - U_D} \tag{3.22b}$$

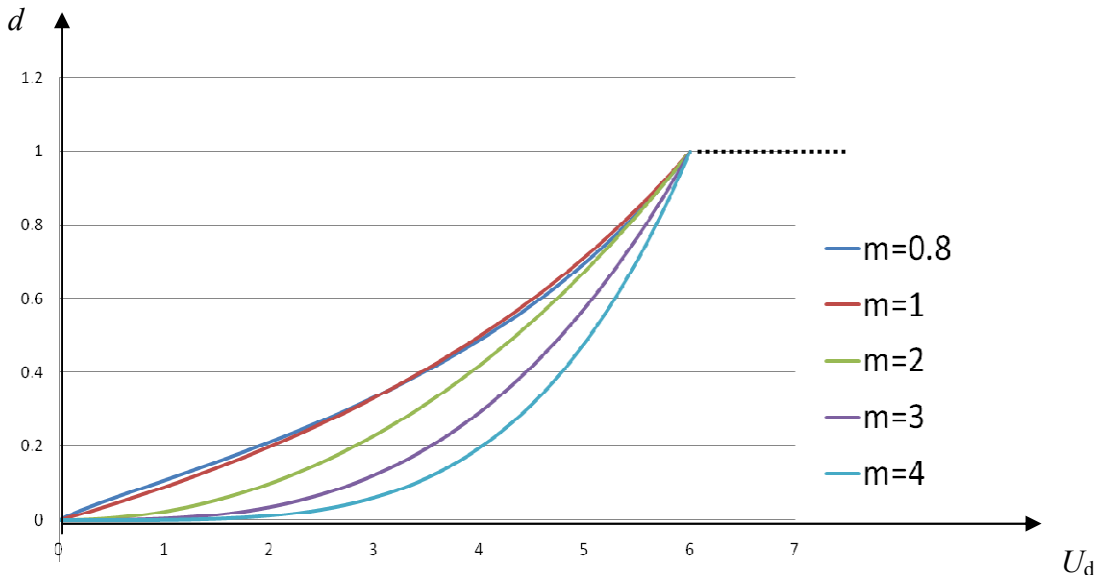

Figure 3.12 Schematic diagram of evolution of damage parameter as a function of dissipated energy

Figure 3.12 shows the evolution of the damage parameters d for different value of m. The value of d starts from 0, following different paths to 1 for complete damage, depending on the value of m. In the case of strain increase monotonically, the value of d also increases monotonically to indicate the damage development. In the case of strain reverse, d will remain at its historically high value. This is to reflect the fact that damage is irreversible in the material. It should be noted that with the change of m value, the expression of d generates different shape of stress-strain curves during the damage evolvement.

3.4 Application to pre-cracked composites

The elastic-plastic damage material model proposed here was implemented in a finite element code ABAQUS/Standard using a user subroutine UMAT. The damage material model is applied to DENT, DCB and INF finite element models under plain strain condition. The DCB and INF tests cover the scenario for stable delamination under pure mode I and II loading, respectively. In both tests, the delamination is assumed to grow in the interlaminar region within the mid-plane. The DENT test is for a model of homogenous property, covering the loading scenarios for Mode I. The stress-strain response under different loading conditions will be obtained by applying appropriate loads and boundary conditions to the FE models. Details of the configurations of these test specimens are given in the subsequent sections.

3.4.1 Double-edge-notched tensile (DENT) test

The computational model shown in Figure 3.13 is for prediction of crack growth in an un-predefined crack path, which consists of homogenous elastic-plastic material. This case study is to demonstrate the use of the proposed elastic-plastic damage material model to simulate damage propagation in an un-predefined crack path. Due to symmetry of geometry and loading condition, only a quarter of the specimen was modeled for the FEM analysis. The quarter-symmetry finite element model is shown in Figure 3.13(b). Geometric detail of the DENT model is given in Table 3.4 and the material property in Table 3.5.

Table 3.4 Geometrical properties used in the DENT model.

U_2	d	a	$L(mm)$	$H(mm)$
1.5	10	35	45	184

Table 3.5 Material properties of solid elements for DENT FE model

Elastic Property		Plastic property			Interlaminar material strength	
E (MPa)	v	σ_y (MPa)	ε^p	U_C (kJ/m^3)	T (MPa)	S (MPa)
3400	0.3	40 200 253.33	0 0.9 1.2	15000.0	72.0	40.0

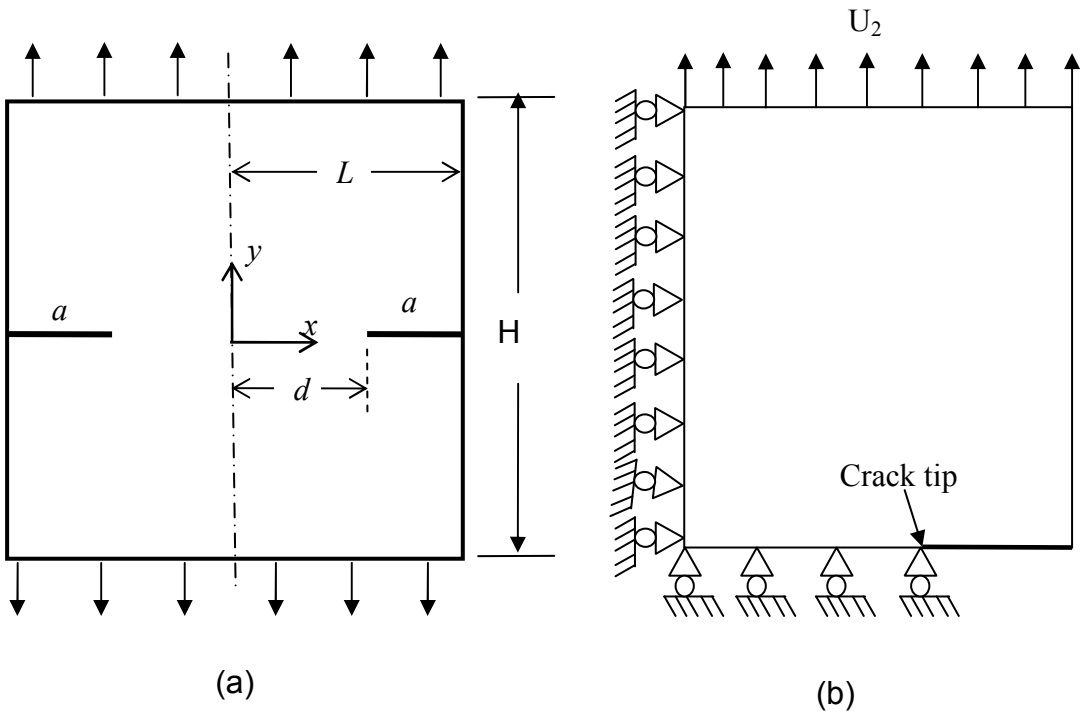

Figure 3.13 DENT test: (a) specimen configuration, and (b) FE model.

The model consists of 7426 plane-strain elements (CPE4) with the elastic-plastic damage material properties. Symmetric boundary conditions were applied along the two axes of symmetry, and a displacement of 1.5mm was applied along the top edge of the model.

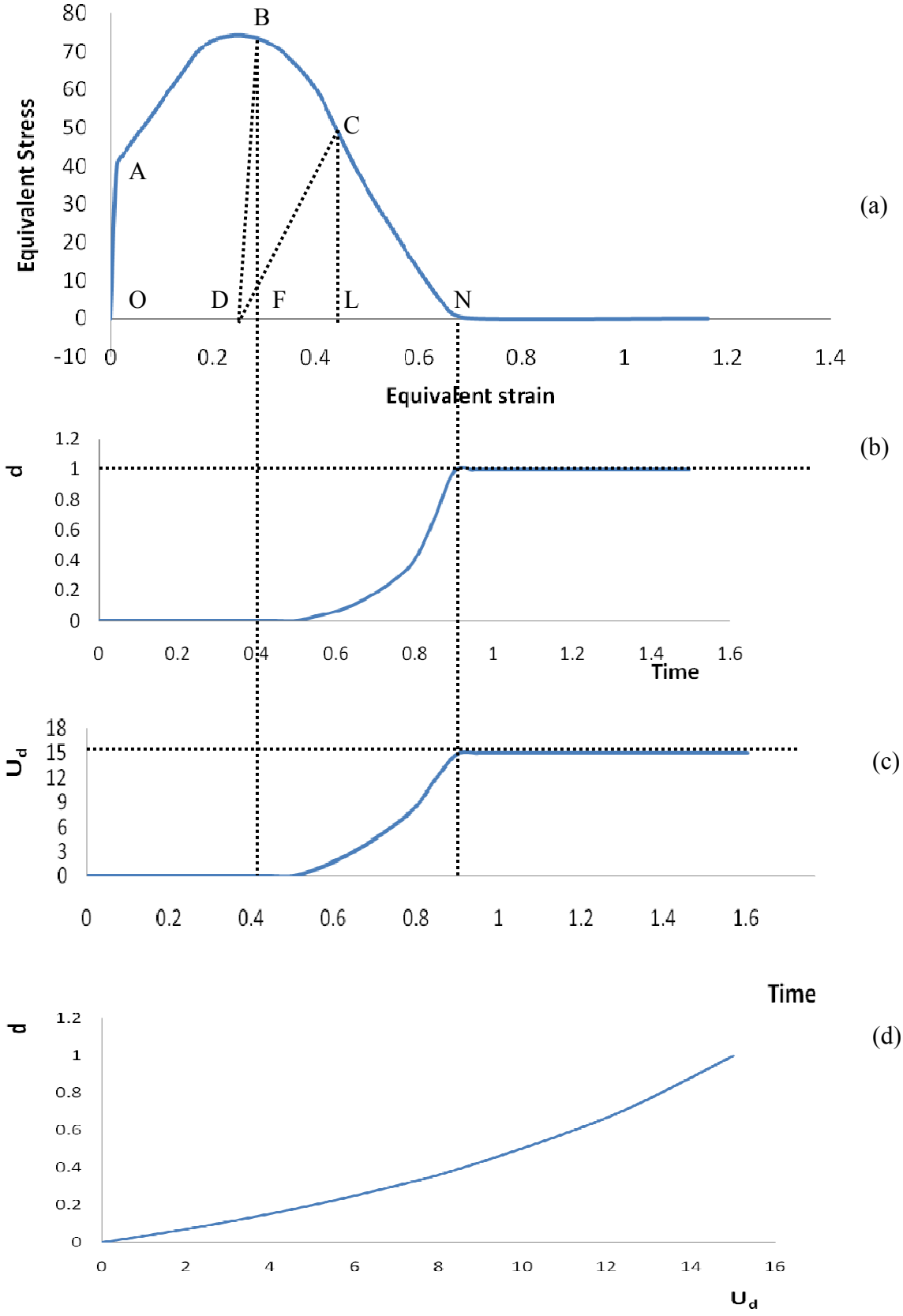

Figure 3.14 Stress-Strain curve and development of damage process in DENT test

Figure 3.14(a) shows the stress-strain relationship of the DENT model subjected to vertical displacement along the top edge. Vertical and horizontal axes of the curve in Figure 3.14(a) represent the equivalent stress (σ_{eq}) and total strain (ε_{eq}), respectively.

Point B in Figure 3.14(a) refers to the moment when the damage initiation criterion is met, i.e. the equivalent stress reaching a critical value of 74MPa and the corresponding equivalent strain 30%. The area DBF equals the strain energy, U_0. Beyond point B the equivalent stress drops gradually with the increase of the equivalent strain.

At any point during damage evolvement, such as point C in Figure 3.14(a), the total input of energy density is the area of OABCL, which can be divided into areas OABD, DBC and DCL, representing the dissipated energy due to plastic deformation, the unrecoverable energy loss due to material damage (U_d) and the recoverable elastic strain energy, respectively. If the applied load on the DENT specimen continues to increase from this point, the load carrying capacity of the element will continue to drop due to decrease of the equivalent stress following the line segment CN, till point N at which unrecoverable energy loss, area DBN, equals U_C. At this point the equivalent stress is zero. Figure 3.15 displays an equivalent stress contour plot to identify the damaged region with zero equivalent stress.

If unloading is applied at point C, the equivalent stress will return to zero linearly following the line segment CD in Figure 3.14(a), at a slope $\overline{E}$ which is determined by Eqn. (3.18).

Figures 3.14(b) and 3.14(c) illustrate the evolution of the damage parameters *d* and the dissipated energy loss (U_d) during the damage process. Both curves in Figures 3.14(b) and (c) start at point B and increase monotonically to point N at which a complete damage

occurred with a critical value of 1 for d and 15kJ for U_d. If unloading occurs during the damage development, d will remain at its historically high value. This is to reflect the fact that damage is irreversible in the material.

As mentioned in section 3.3.3 and shown in Figure 3.12, changing the expression for d (Eqn. (3.20(a))) could yield different shapes of stress-strain responses. The stress-strain behavior of which shown in Figure 3.14(a) is obtained by using the expression for d given by Eqn. (3.20(b)). Figure 3.14(d) shows the evolution of the damage parameter as a function of the dissipated energy U_d during the damage process. Figures 3.16 (a) and (b) display a contour plot of damaged elements and crack growth direction in the DENT FE model with fine and course mesh density. It also shows that the prediction of the crack growth is insensitive to the mesh size. However, the finite element model with finer mesh results in more accurate solution as expected.

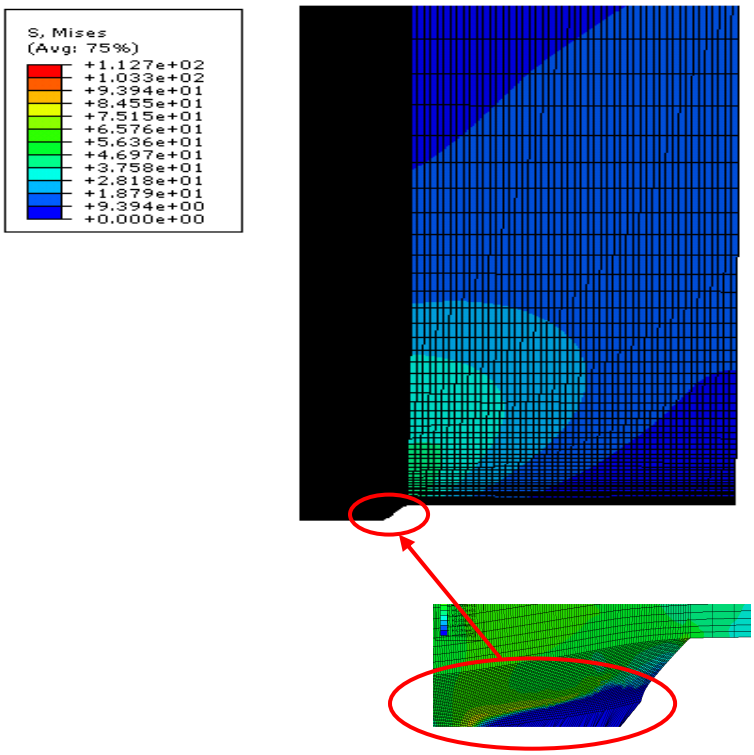

Figure 3.15 Contour plot of equivalent stress in DENT model

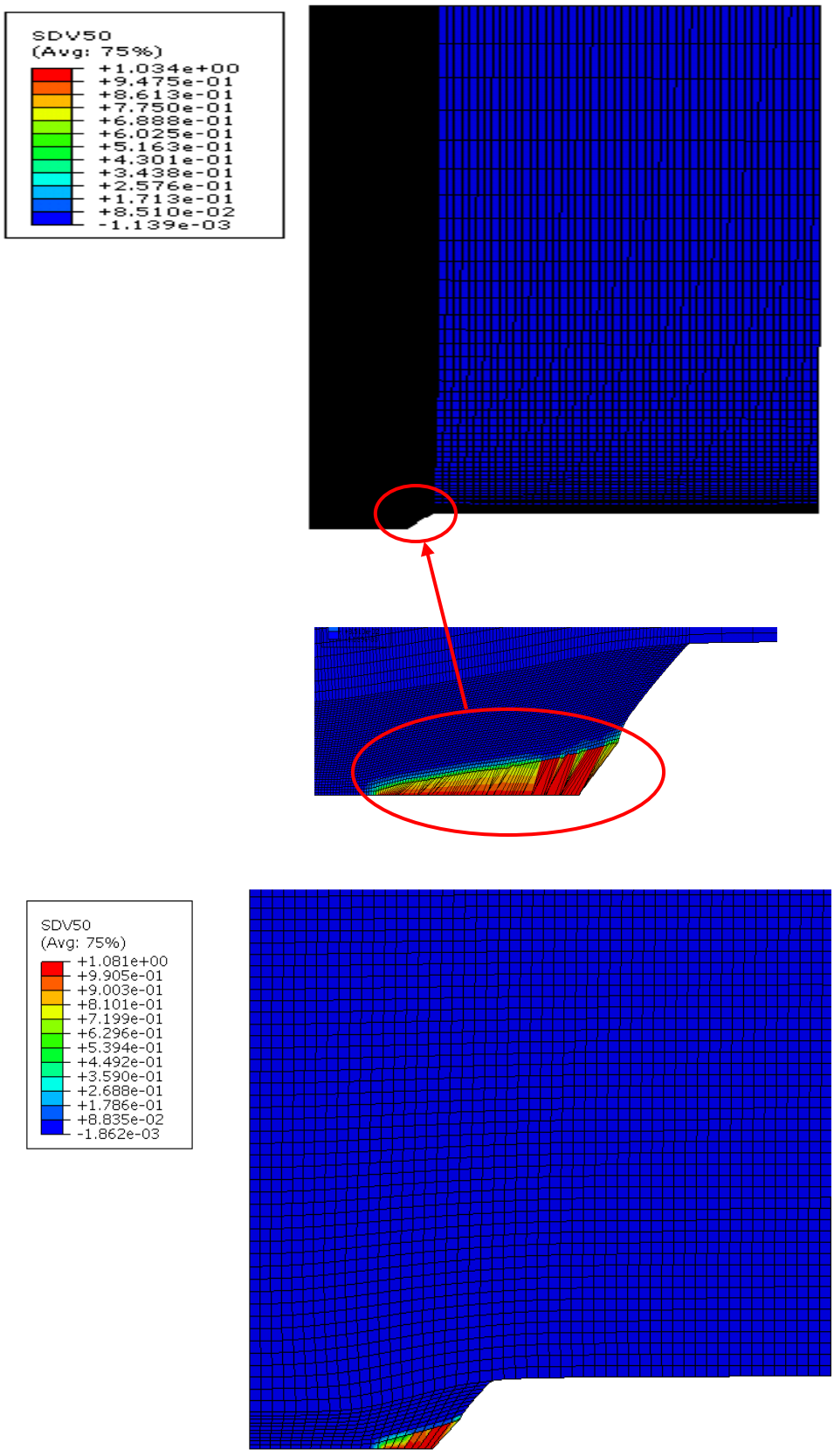

Figure 3.16 Contour plot of damaged elements and crack growth in DENT model (a) fine mesh (b) course mesh

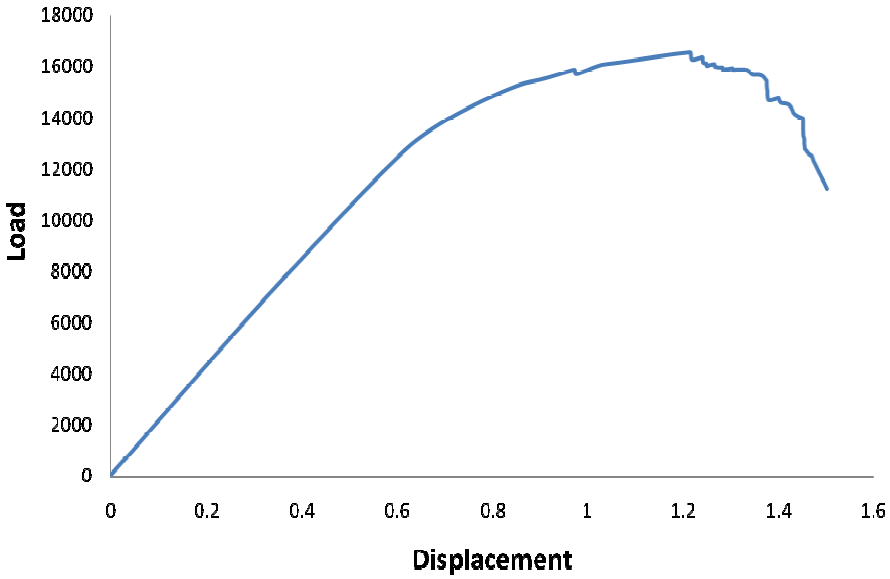

Figure 3.17 Load-displacement curve for the DENT test

Figure 3.17 demonstrates the load-displacement curve of DENT specimen from FE simulation. The initial linear curve indicates that the load increased linearly with displacement until it reaches 12000N and represents the elastic region. After a smooth transition from the elastic region with nonlinear response, which indicates the occurrence of local plasticity, the load continues to increase in the yielding section before a critical loading level was reached to cause the damage initiation. After a critical load of 15871N was reached, the load drops gradually with the damage growth.

3.4.2 Delamination Growth in Double Cantilever Beam (DCB) test

The DCB model shown in Figure 3.18 is studied to demonstrate the elastic-plastic damage material model for simulating stable delamination propagation under mode I loading condition. The FE model of the DCB specimen has three layers and the overall dimensions of the model are listed in Table 3.6. Top and bottom layers represent

substrates of the composite material, consisting of 4-node plane-strain elements (CPE4R) of orthotropic elastic properties. The middle layer represents the interlaminar region which includes initial crack lengths of 50 mm. The un-cracked region in the middle layer consists of 4-node, plane-strain continuum solid elements (CPE4R) with the elastic-plastic damage material property. The model contains a total of 6256 elements. Element length in the interlaminar region was chosen to be 0.02 mm. According to Turon et al. [30], element length in the cohesive damage zone should be small enough to capture the continuum stress field in this region. Therefore, the mesh size should be sufficiently small to provide good resolution for the stress distribution.

Figure 3.18 shows the mesh pattern and prescribed boundary conditions of the finite element model. Input material properties for the top and bottom layers are given in Table 3.7, and those for the middle layer in Table 3.8 which are to define constitutive equation of the continuum solid elements based on an elastic-plastic damage material model.

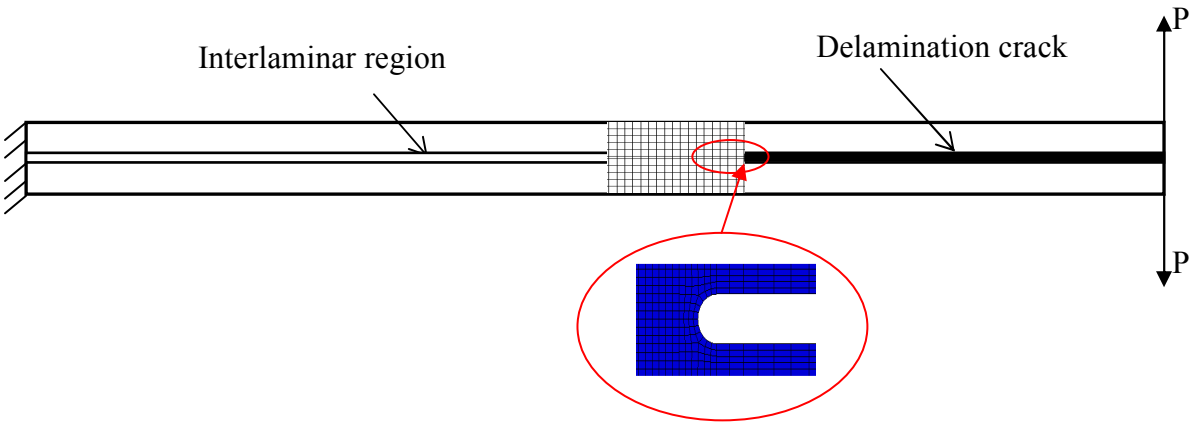

Figure 3.18 Schematic diagram of finite element model for DCB specimen with mesh details at crack tip

Table 3.6. Dimensions of the FE model of DCB specimen

a (mm)	h (mm)	L (mm)	w (mm)
50	1.5	150	20

Table 3.7. Mechanical properties for top and bottom layers of the DCB FE model used in this study

E_{11} (GPa)	$E_{22} = E_{33}$ (GPa)	$G_{12} = G_{13}$ (GPa)	ν_{23}	$\nu_{12} = \nu_{13}$
150	11.0	6.0	0.3	0.3

Table 3.8 Properties of solid elements in the interlaminar region of the DCB FE model

Elastic Property		Plastic property			Interlaminar material strength	
E (MPa)	ν	σ_y (MPa)	ε^p	U_C (kJ/m^3)	T (MPa)	S (MPa)
3400	0.3	40 200 253.33	0 0.9 1.2	5000.0	20.0	20.0

Contour plots of equivalent stress and damage level around the crack tip are shown in Figure 3.19 by applying the elastic-plastic damage material model to the inter-laminar region. Due to loading symmetry and boundary conditions in the DCB specimen, the delamination is expected to start from the mid plane, which is indeed indicated by Figure 3.19(b) and 3.19(c). This supports that the proposed damage material model can accurately predict the delamination growth path in the DCB specimen. Figure 3.20 presents the FE results when the elastic-plastic damage material property in Table 3.8, is

applied to the entire DCB model. However, because of a sever distortion of the damaged elements around the crack front, simulation cannot proceed further for the crack growth. Since there will not be interfacial penetration between the adjacent delaminated surfaces under mode I loading, those highly distorted damaged elements that do not take any load (stress) could be deleted from the FE model to advance the simulation. Because of the use of UMAT subroutine in ABQUS/Standard which doesn't support element deletion in real time during the simulation, this problem couldn't be solved and require further study in the future.

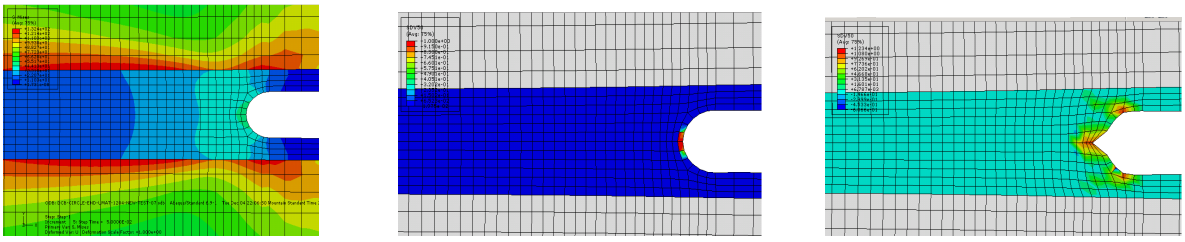

(a) (b) (c)

Figure 3.19 FE result of DCB test with the proposed damage material applied to the interlaminar region: (a) Contour plot of equivalent stress on FE model (b) contour plot of damage level around the crack tip in the early stage, (c) contour plot of the damage level around crack tip during the delamination growth

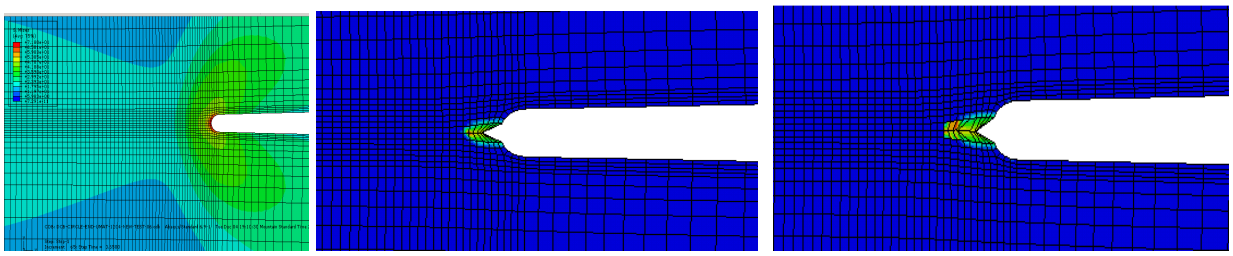

(a) (b) (c)

Figure 3.20 FE results of DCB specimen with the proposed damage material property applied to the entire FE model: (a) Contour plot of equivalent stress, (b) contour plot of damage parameter around crack tip at the early stage, and (c) contour plot of the damage parameter around the crack tip during the delamination growth.

3.4.3 Delamination Growth in INF Specimen Under three-point bending

Delamination growth in the INF model, as shown in Figure 3.21, is studied using continuum solid elements with elastic-plastic damage material property. Similar to the previous DCB model, the FE model of the INF specimen has three layers and the overall dimensions of the model are listed in Table 3.1. Top and bottom layers represent substrates of the composite material, consisting of 4-node plane-strain elements (CPE4I) with incompatible mode of orthotropic elastic properties. The middle layer represents the interlaminar region which includes initial crack lengths of 40 mm for a_1 and 12 mm for a_2. The un-cracked region in the middle layer consists of 4-node, plane-strain continuum solid elements (CPE4R) with the elastic-plastic damage material property. Totally, 10421 elements were used for the top and bottom layers, and 6540 elements for the middle layer. A frictionless, small sliding contact is defined between the crack surfaces to avoid penetration. The specimen is subjected to a displacement of 4mm at the central loading pin. A frictionless and small sliding contact condition is defined in the pre-cracked

surfaces. The nodal points at the two supporting pins were restricted from any vertical motion during the delamination growth. Besides, the nodal point at the left support was constrained from any horizontal movement to avoid rigid body motion. Input material properties for the top and bottom layers are given in Table 3.2, and those for the middle layer in Table 3.9 which are for defining constitutive equation of the continuum solid elements based on an elastic-plastic damage material model.

Table 3.9 Properties of solid elements at the interlaminar interface of the INF FE model

Elastic Property		Plastic property		Interlaminar material strength		
E (MPa)	v	σ_y (MPa)	ε^p	U_C (kJ/m^3)	T (MPa)	S (MPa)
3400	0.3	40	0	5000.0	72.0	40.0
		200	0.9			
		253.33	1.2			

Material properties chosen for the interlaminar region, such as tensile (T) and shear (S) strengths, are based on properties of the resin used in the simulation. The critical strain energy (U_C), yield stresses and equivalent plastic strains are virtual data for the purpose of testing the proposed damage model.

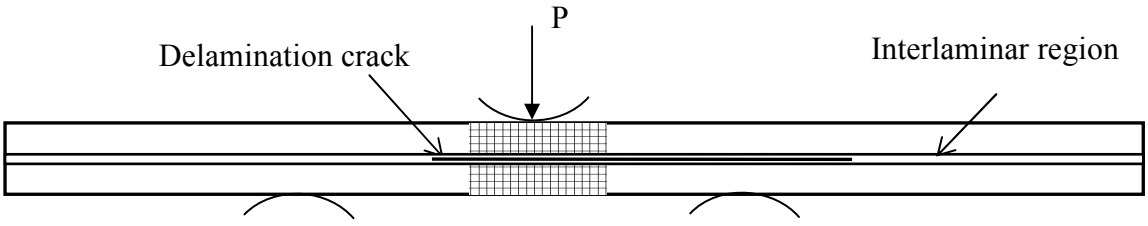

Figure 3.21 Finite element model of INF test

The results from the 2D model are given in Figures 3.22-3.24. Distribution of the equivalent stress in Figure 3.22 shows the highest stress concentration at the interface between the outer substrate and the interlaminar region. Such a stress concentration is probably caused by the mismatch of material property at the interface and can cause damage initiation from corners of the crack tip. To minimize such stress concentration effect, the crack tip is modeled with circular profile within the interlaminar region. Figures 3.23 demonstrates the deformed shape in front of the crack tip, resulting in compression on the top half and tension on the bottom half of the interlaminar region. Figures 3.24 show the location of damage initiation along the contour of the crack tip and its growth path in the interlamianr region. It is interesting to note that the crack initiation and its growth path from the crack tip are influenced by the values of the tensile and shear strengths of the material in the interlaminar region. In figure 3.24(a), the crack initiation occurs a little below the top corner of the crack tip and subsequently the crack grows in the interlaminar region. In this case the crack initiation is probably caused by shear failure of the material, not the tensile failure. When the tensile strength of the material is lower than its shear strength as shown figure 3.24(b) and 3.24(c), the crack initiation occurs around the bottom corner of the crack tip. This may be caused by tensile failure of the material, not the shear failure. Such initiation of local crack due to tensile failure in a mode II loading test was also reported in ref. [32]. Further study is required to examine the effect of material tensile and shear strengths on the damage initiation for delamination. In figure 3.24(c), the crack grows towards the substrate/matrix interface.

Similar to the FE results for the DCB specimen, distortion of damaged elements due to high plastic strain in the INF specimen model causes instabilities and inhibits

further crack growth progress. However, unlike the DCB specimen, care has to be taken when removing those highly distorted elements from the INF test as this may cause penetration between adjacent delaminated surfaces. Since the fully damaged elements in the INF specimen can still take compressive forces to avoid penetration, due to, removing those elements may increase cause penetration. Another problem from deleting elements in the INF test is the contact condition. When new fracture surfaces are created after deleting the elements, the contact algorithm in ABAQUS has to calculate new contact surfaces, and the associated contact forces, which may cause numerical instabilities. This suggests that the contact calculation is much easier if elements were not required to be deleted. All of those problems need further investigation.

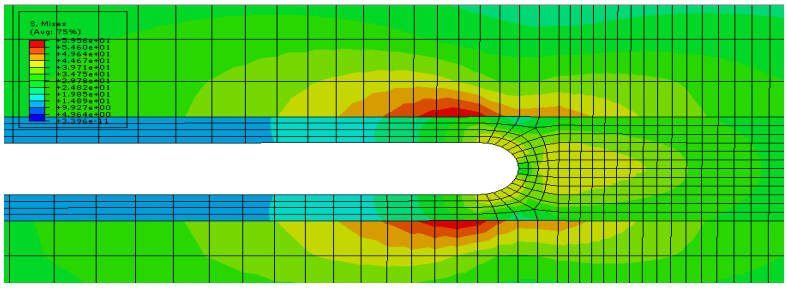

Figure 3.22 Contour plot of equivalent stress distribution in INF test

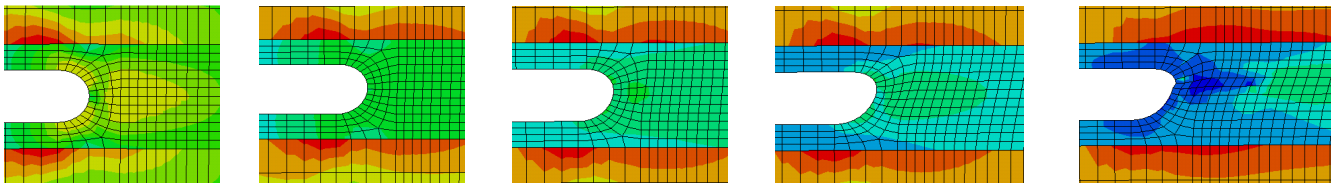

(a) (b) (c) (d) (e)

Figure 3.23 Contour plot of equivalent stress around crack tip in the INF test with T=70MPa and S=40MPa

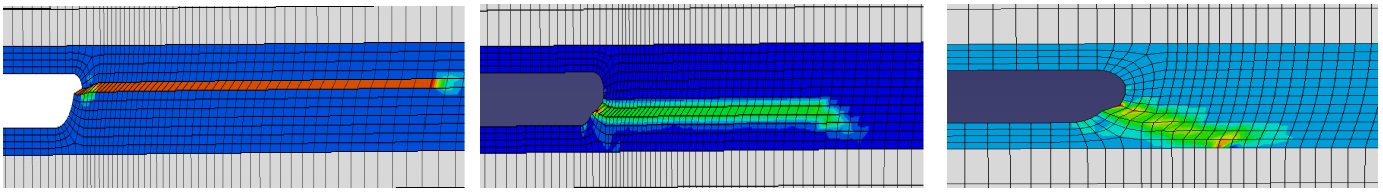

(a) (b) (c)

Figure 3.24 Contour plot of damage parameter in the INF specimen with (a) T=70MPa and S=40MPa (b) T=30MPa and S=40MPa (c) T=25MPa and S=40MPa

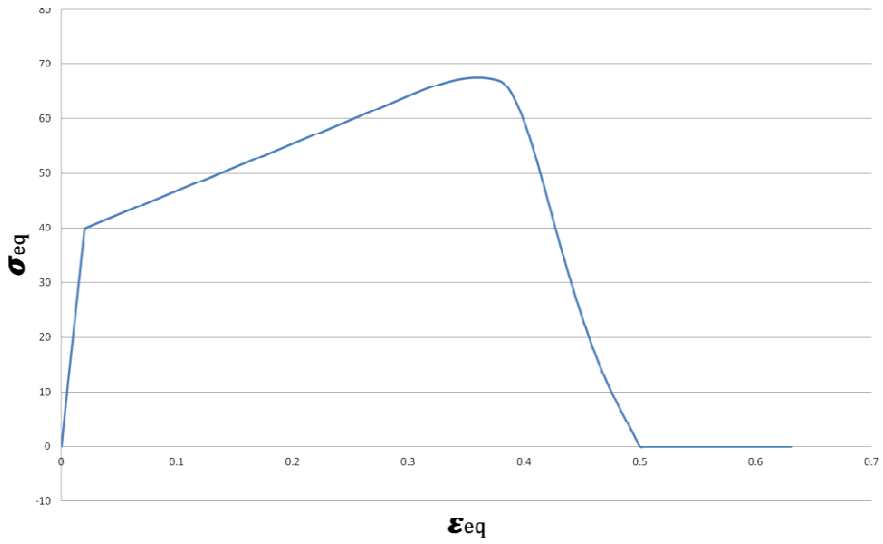

Figure 3.25 Stress-strain curve of INF model from FE simulation

Figure 3.25 shows the stress-strain response of the INF model obtained by applying three-point bending with properties given in Tables (3.1), (3.2) and (3.9). The curve profile is similar to the stress-strain curve of the DENT specimen presented in the earlier sections.

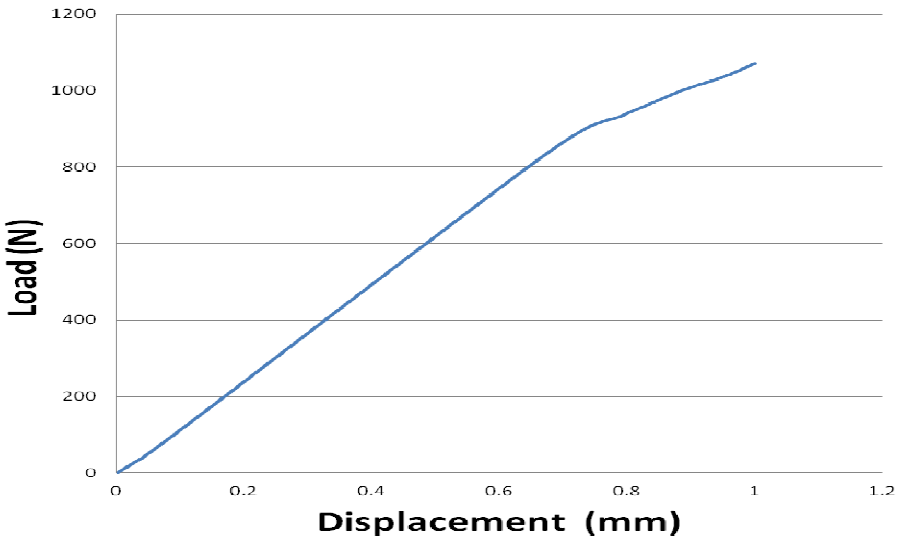

Figure 3.26 Load-displacement curve of INF model from FE solution

Figure 3.26 shows load-displacement curves from the FEM simulation, which indicates that the load increases linearly with displacement before delamination commences and continues to increase linearly with the displacement during the delamination growth at a smaller slope. This suggests a stable delamination growth.

3.5 Conclusions

This chapter presents a finite element approach based on a continuum solid element with an elastic-plastic damage material property to simulate delamination growth in the interlamianr region of FRP. Taking the advantage of solid element in terms of simplicity and true representation for the stress state over other elements such as interface or spring elements, a FE model using continuum solid elements can adopt a criterion that considers all possible combinations of stresses for crack initiation. In this study, a combination of stresses that takes into account the effect of in-plane normal stress was proposed for the damage initiation. The fracture criterion is defined based on critical

strain energy. The proposed damage material model was implemented in finite element code ABAQUS and was applied to pre-cracked composites to verify the damage criteria. It is shown that with a simple linear softening function for the damage evolution, the proposed damage material model can predict the delamination development in a pure mode of fracture in fiber composites. The elastic-plastic damage material model was applied to pre-cracked composite structures such as the DCB, INF and DENT tests.

Chapter 4 Conclusions and Future Work

4.1 Summary and Conclusions

Methodologies are discussed for the prediction of stable delamination development in fiber-reinforced composites in pure mode II fracture using analytical and numerical methods. Analytical and numerical approaches are described to quantify critical energy release rate, which is the parameter to measure delamination resistance of the composites.

This thesis presented a revised analytical approach for calculating the compliance of the INF test by taking into account loads in the overhanging section of the specimen. The work shows improvement of the revised analytical solution in its accuracy in predicting the delamination growth, by taking into account the loads in the overhanging section. Therefore, the work concludes that the overhanging section cannot be ignored. The revised analytical solution was also used to explore the influence of load in the overhanging section on prediction of delamination growth rate generated in the INF specimen. The results suggest that the delamination growth rate in the INF test is proportional to the loading rate, thus making it possible to investigate the effect of the crack growth speed on the critical energy release rate.

The finite element model of a virtual INF specimen was used to validate the revised expressions for compliance and energy release rate through comparison of the initial specimen stiffness of both solutions. The INF specimen had cohesive elements in the interlaminar region to simulate the delamination growth, from which extent of damage

in front of the crack tip was quantified. Results from FE model suggested that an extensive damage exists at the crack tip before delamination growth commences. The FE model, suggests that the damage zone has a length of 8mm which should effectively extend the initial crack length. Therefore, the use of a physical crack length to calculate the energy release rate may severely overestimate the interlaminar fracture toughness. Hence, an effective crack length, which considers the additional crack length due to the presence of a damage zone at the crack tip, was used to predict the delamination growth. Expression for the energy release rate based on the effective crack length yields a value that is very close to the input critical energy release rate (G_c) input into the cohesive elements.

A finite element approach based on a continuum solid element with an elastic-plastic damage material property was proposed to simulate delamination growth in the interlamianr region of FRP. Using solid elements, a combination of stresses that takes into account the effect of in-plane normal stress was used to establish the criterion for damage initiation. The criterion for delamination propagation is defined based on critical strain energy. The proposed damage material model was implemented in finite element code and was applied to pre-cracked composites to illustrate its feasibility to simulate the crack development.

In general, the work has successfully used analytical and numerical approaches to simulate delamination growth in FRP under pure mode II loading.

4.2 Future work

Verification of the present damage material approach is still in a preliminary stage and currently, only applied to pre-cracked composite structures. This approach will be applied to composites with no pre-cracks to further verify its feasibility and the proposed damage initiation criteria. Parametric studies will also be carried out using appropriate test methods to investigate the influence of material strengths and other parameters on the simulation results.

Additionally, mixed-mode delamination is not addressed in this study, which is a natural next step for the investigation. Besides, a strategy should be devised to measure delamination resistance experimentally. In the proposed elastic-plastic damage material model, the damage initiation criteria and the fracture criterion for delamination evolution are all based on 3D stress and energy state. Thus, this approach could be extended to 3D simulations, but a strategy is needed to separate the fracture modes involved in the crack growth.

References

1. Anon. Farnborough 2004 - Good prospects for aerospace composites. *Reinforced Plast* 2004; 48(8): 42-46. D.J. Wilkins, J.R. Eisenmann, R.A. Camin, W.S. Margolis and R.A. Benson, "Characterizing Delamination Growth in Graphite-Epoxy, Damage in Composite Materias," ASTM-STP-775, 1982, 168-183.
2. Camanho, P.P., Mathews, F.L., 1999 "Delamination onset prediction in mechanically fastened joints in composite laminates" J. Compos. Mater. 33, 906-927
3. Wang Y, Williams JG. Corrections for Mode II fracture toughness specimens of composites materials. *Composites Sci Technol* 1992; 43(3): 251-256.
4. Salpekar SA, Raju IS, O'Brien TK. Strain energy release rate analysis of the end-notched flexure specimen using the finite-element method. *J Composites Technol Res* 1988; 10(4): 133-9.
5. Xie D, Waas AM, Shahwan KW, Schroeder JA, Boeman RG. Computation of energy release rates for kinking cracks based on virtual crack closure technique. *CMES - Computer Modeling in Engineering and Sciences* 2004; 6(6): 515-524.
6. Shih CF, Needleman A. Fully plastic crack problems. I. Solutions by a penalty method. *Transactions of the ASME Journal of Applied Mechanics* 1984; 51(1): 48-56.
7. Shih CF, Needleman A. Fully plastic crack problems. II. Application of consistency checks. *Transactions of the ASME Journal of Applied Mechanics* 1984; 51(1): 57-64.

8. A. Turon, P.P. Camanho, J. Costa, C.G. Davila. A damage model for the simulation of delamination in advanced composites under variable-mode loading. Mechanics of Materials 38(2006), 1072-1089
9. Z. Zou, S.R. Reid, S. Li. A continuum damage model for delamination in laminated composites. Journal of the Mechanics and Physics of Solids 51(2003) 333-356
10. Alfano G, Crisfield MA. Finite element interface models for the delamination analysis of laminated composites: Mechanical and computational issues. *Int J Numer Methods Eng* 2001; 50(7): 1701-1736.
11. ASTM D5528-01, "Standard Test Method for Mode I Interlaminar Fracture Toughness of Unidirectional Fiber-Reinforced Polymer Matrix Composites," Annual Book of ASTM Standards, Vol. 15.03, 2004.
12. O'Brien, T.K., "Interlaminar Fracture Toughness: The long and winding road to standardization," Composites Part B: Engineering, Vol.29, No.1, 1998, pp.57-62.
13. B.R.K Blackman, A.J. Brunner, J.G. Williams, "Mode II fracture testing of composites: a new look at an old problem," Engineering Fracture Mechanics 73(2006) 2443-2455.
14. C. Fan, P.-Y. B. Jar, J.J. R. Cheng, "Mode II delamination toughness in glass fiber-reinforced polymers with bridging fibers and stitching threads," J.Reinforced Plastics and Composites 28(14),1689-1703(2009).
15. H.Maikuma, J.W. Gillespie, and J.M. Whitney, "Analysis and Experimental Characterization of the Center Notch Flexural Test Specimen for Mode II Interlaminar Fracture,"*J Composite Mater,* **23**(8): 756-86.

16. C. Fan, P.-Y. B. Jar, J.J. R. Cheng, “Energy-based analysis of delamination development in fiber-reinforced polymers (FRP) under 3-point bending test” Compos. Sci.Tech.66,2143-2155(2006).
17. E.Reissner, “The Effect of Shear Deformation on the Bending of Elastic Plates,” J. Appl. Mech. 12(1945) A-69.
18. Anderson TL. Fracture Mechanics of Polymers. 2nd ed. Florida: CRC Press LLC; 1995
19. Schuecker, C. and Davidson, B.D.(2000). Evaluation of the Accuracy of the Four-point Bend End-notched Flexure Test for Mode II Delamination Toughness Determination, Composites Science and Technology, 60: 2137-2146.
20. Alfano G, Crisfield MA. Finite element interface models for the delamination analysis of laminated composites: Mechanical and computational issues. *Int J Numer Methods Eng* 2001; 50(7): 1701-1736.
21. Blackman BRK, Hadavinia H, Kinloch AJ, Williams JG. The use of a cohesive zone model to study the fracture of fibre composites and adhesively-bonded joints. *Int J Fract* 2003; 119(1): 25-46.
22. Qiu Y, Crisfield MA, Alfano G. An interface element formulation for the simulation of delamination with buckling. *Eng Fract Mech* 2001; 68(16): 1755-76.
23. Mi Y, Crisfield MA, Davies GAO, Hellweg H-. Progressive delamination using interface elements. *J Composite Mater* 1998; 32(14): 1246-1272.
24. Turon A, Camanho PP, Costa J, Davila CG. (2004). Interface Damage Model for the Simulation of Delamination Under Variable-Mode Ratio in Composite Materials. Report No.: NASA/TM-2004-213277. United States: .

25. Turon A, Davila CG, Camanho PP, Costa J. (2005). Engineering Solution for Using Coarse Meshes in the Simulation of Delamination with Cohesive Zone Models. Report No.: NASA/TM-2005-213547. United States: .
26. Chengye Fan. Characterization and Prediction of Delamination in Fiber-reinforced Composites. PhD Dissertation, Department of Mechanical Engineering, University of Alberta 2007.
27. Chengye Fan, P. –Y. Ben Jar, J.J. Roger Cheng. Cohesive zone with continuum damage properties for simulation of delamination development in fiber composites and failure of adhesive joints. *Engineering Fracture Mechanics* 75(2008) 3866-3880.
28. ABAQUS Version 6.9
29. J.P. Hou, N. Petrinic, C. Ruiz, S.R. Hallett. Prediction of impact damage in composite plates. Composite Science and Technology 60(2000) 273-281.
30. Turon A, Davila CG, Camanho PP, Costa J. (2005). Engineering Solution for Using Coarse Meshes in the Simulation of Delamination with Cohesive Zone Models. Report No.: NASA/TM-2005-213547. United States:
31. Benzeggagh, M.L. and M. Kenane. Measurement of Mixed-Mode Delamination Fracture Toughness of Unidirectional Glass/Epoxy Composites with Mixed-Mode Bending Apparatus. Composites Science and Technology 56(1996) 439-449.
32. M. Todo, P.-Y.B. Jar, K. Takahashi. Initiation of a mode-II interlaminar crack from an insert film in the end-notched flexure composite specimen. Composites Science and Technology 60(2000) 263-272.
33. Qiang Xu, Zixing Lu. An elastic-plastic cohesive zone model for metal-ceramic interfaces at finite deformations. International Journal of Plasticity 41(2013) 147-164.

34. Song Xin, Liu Zheng, Zhang Jiazhen. Simulation study of fracture behavior in a FML specimen by 3D elastic-plastic finite element model. Polymers and Polymer Composites, 19(2011) 209-212.